Article

Cell Reports

Reciprocal TCR-CD3 and CD4 Engagement of a Nucleating pMHCII Stabilizes a Functional Receptor Macrocomplex

Graphical Abstract

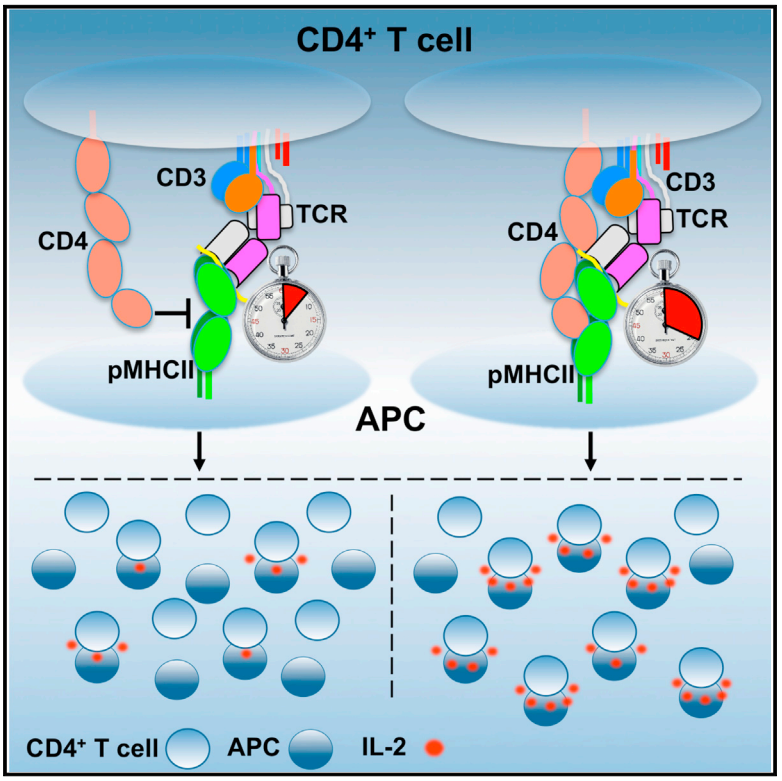

Highlights

- The affinity of TCR-pMHCII interactions impacts CD4 confinement to MHCII
- CD4 increases the duration of TCR-pMHCII interactions in the absence of signaling
- The CD4 D1 and D3 domains contribute to macrocomplex stability and functionality

Authors

Caleb R. Glassman, Heather L. Parrish, Mark S. Lee, Michael S. Kuhns

Correspondence

mkuhns@email.arizona.edu

In Brief

Glassman, Parrish et al. use functional and biophysical assays to demonstrate that CD4 stabilizes TCR-pMHCII interactions via membrane distal and proximal domains. The data indicate that CD4 docks along a composite surface created by the TCR-CD3-pMHCII axis to confer a uniform macrocomplex architecture upon a diverse TCR repertoire.

Glassman et al., 2018, Cell Reports *22*, 1263–1275
January 30, 2018
https://doi.org/10.1016/j.celrep.2017.12.104

CellPress

Cell Reports
Article

Reciprocal TCR-CD3 and CD4 Engagement of a Nucleating pMHCII Stabilizes a Functional Receptor Macrocomplex

Caleb R. Glassman,[1,5,6] Heather L. Parrish,[1,5] Mark S. Lee,[1] and Michael S. Kuhns[1,2,3,4,7,*]
[1]Department of Immunobiology
[2]The BIO-5 Institute
[3]The Arizona Center on Aging
[4]The University of Arizona Cancer Center
The University of Arizona College of Medicine, Tucson, AZ 85724, USA
[5]These authors contributed equally
[6]Present address: Program in Immunology, Stanford University School of Medicine, Stanford, CA 94305, USA
[7]Lead Contact
*Correspondence: mkuhns@email.arizona.edu
https://doi.org/10.1016/j.celrep.2017.12.104

SUMMARY

CD4$^+$ T cells convert the time that T cell receptors (TCRs) interact with peptides embedded within class II major histocompatibility complex molecules (pMHCII) into signals that direct cell-fate decisions. In principle, TCRs relay information to intracellular signaling motifs of the associated CD3 subunits, while CD4 recruits the kinase Lck to those motifs upon coincident detection of pMHCII. But the mechanics by which this occurs remain enigmatic. In one model, the TCR and CD4 bind pMHCII independently, while in another, CD4 interacts with a composite surface formed by the TCR-CD3 complex bound to pMHCII. Here, we report that the duration of TCR-pMHCII interactions impact CD4 binding to MHCII. In turn, CD4 increases TCR confinement to pMHCII via reciprocal interactions involving membrane distal and proximal CD4 ectodomains. The data suggest that a precisely assembled macrocomplex functions to reliably convert TCR-pMHCII confinement into reproducible signals that orchestrate adaptive immunity.

INTRODUCTION

CD4$^+$ T cells are remarkable for their sensitivity, specificity, and the range of effector types to which a naive cell can differentiate after detecting a threat (i.e., helper [Th], T follicular helper [Tfh], regulatory [Treg], and memory [Tm]) (Zhu et al., 2010). The quantity and quality of signals generated by the T cell receptor (TCR) are key determinants for CD4$^+$ T cell development, activation, differentiation, and effector cell responses (Allison et al., 2016; Corse et al., 2010; Fazilleau et al., 2009; Gottschalk et al., 2010; Hwang et al., 2015; Savage et al., 1999; Stepanek et al., 2014; Tubo et al., 2013; van Panhuys et al., 2014; Vanguri et al., 2013). But the genesis of these signals remains unclear because the relationship between the TCR and CD4 remains mechanistically undefined.

Each clonotypic TCR provides a CD4$^+$ T cell with specificity for a limited number of peptides presented within class II major histocompatibility complex (pMHCII) molecules on antigen-presenting cells (APCs). The time a TCR spends confined to a pMHCII informs CD4$^+$ T cell responsiveness. For interactions with slow on-rates, such that newly dissociated TCRs and pMHCII diffuse away from each other before rebinding, this equates to their $t_{1/2}$; however, for TCRs with on-rates that allow rebinding, responsiveness best relates to the aggregate $t_{1/2}$ (t_a) that considers rebinding as part of a total confinement time (Govern et al., 2010; Tubo et al., 2013; Vanguri et al., 2013).

TCR-pMHCII interactions relay information to the immunoreceptor tyrosine-based activation motifs (ITAMs) of the associated CD3$\gamma\varepsilon$, CD3$\delta\varepsilon$, and CD3$\zeta\zeta$ signaling modules (Gil et al., 2002; Lee et al., 2015); however, transmitting information across the membrane to the ten ITAMs within a TCR-CD3 complex (one per CD3γ, δ, and ε subunit, and three per ζ) is insufficient to generate chemical signals because the complex itself lacks intrinsic kinase activity. Rather, the Src kinase p56^{Lck} (Lck), which non-covalently associates with CD4, primarily phosphorylates the ITAMs (Malissen and Bongrand, 2015).

CD4 is critical for TCR-CD3 signaling to single agonist pMHCII, increases functional responses by 10- to 1,000+-fold and determines how a T cell perceives the potency of a pMHCII (Glaichenhaus et al., 1991; Irvine et al., 2002; Killeen and Littman, 1993; Parrish et al., 2016; Stepanek et al., 2014; Vidal et al., 1999). When a CD4 molecule associated with Lck binds the same pMHCII as a TCR, it is thought to recruit Lck to phosphorylate the ITAMs (Malissen and Bongrand, 2015). In this scenario, CD4 is a constant, binding to a monomorphic region of MHCII regardless of the nature of the peptide embedded therein, and thus regardless of whether or not the TCR is bound to the pMHCII.

But three pieces of evidence raise questions about how, upon TCR-pMHCII engagement, CD4 positions Lck and the ITAMs in a sufficient local concentration for a sufficient duration for phosphorylation to occur; particularly for the weak interactions that

drive positive selection and peripheral homeostasis (Glassman et al., 2016; Kao and Allen, 2005; Stepanek et al., 2014; Wang et al., 2001b; Zuñiga-Pflücker et al., 1989). First, crystallography data suggest that the TCR-CD3 complex, pMHCII, and CD4 adopt a V-like arch that could place the CD3 ITAMs, and, in particular, the six ITAMs of ζζ, ~100Å from a CD4-associated Lck (Wang et al., 2001a; Yin et al., 2012). Second, interactions between the CD4 D1 domain and MHCII at the apex of this arch are too weak to measure in solution, and 2D affinity estimates suggest that CD4-MHCII interactions are ~2–3 orders of magnitude weaker than TCR-pMHCII interactions (Hong et al., 2015; Jönsson et al., 2016). Finally, C-terminally truncated CD4 molecules that lack the cysteine clasp, and cannot directly interact with Lck, nevertheless increase TCR-CD3 signaling (Killeen and Littman, 1993; Parrish et al., 2016; Vidal et al., 1999). A unifying understanding of how the TCR-CD3 complex, pMHCII, and CD4 fit and work together thus remains elusive.

Here, we tested predictions made by a V-like macrocomplex versus a more compact architecture in which CD4 docks along a composite surface formed by the TCR-CD3-pMHCII axis (Figure S1A) (Glassman et al., 2016; Kuhns and Badgandi, 2012; Wang et al., 2001a; Yin et al., 2012). In the latter model, TCR-CD3 dwell time on pMHCII would determine the duration with which the CD4 docking site is formed and thus influence CD4 dwell time within a mature macrocomplex. In turn, CD4 docking would extend the TCR-CD3 dwell time on pMHCII. Neither would occur in the V-like arch since TCR-pMHCII and CD4-MHCII interactions are independent of one another. Finally, in the V-like arch CD4 binds MHCII only via the D1 domain, while CD4 would use its length to contact the TCR-CD3-pMHCII axis in a compact macrocomplex. To test these predictions, we varied the duration of TCR-pMHCII interactions with defined altered peptide ligands (APLs), and the duration of CD4-MHCII interactions with a CD4 D1 domain mutant, to study how these changes influenced the interplay between the TCR-CD3 complex and CD4 upon binding pMHCII. We also made mutants in the CD4 D3 domain. The data suggest that reciprocal interactions between the TCR-CD3 complex and CD4 ectodomains around a nucleating pMHCII impact the assembly, stability, and function of the TCR-CD3-pMHCII-CD4 macrocomplex.

RESULTS

CD4 Enhances Functional Responses to Low-Affinity pMHCII

This study was designed to evaluate the interplay between the TCR-CD3 complex and CD4 by testing predictions made by the V-like arch and compact macrocomplex models (Figure S1A). We primarily used the archetypal cytochrome-*c*-reactive 5c.c7 TCR since there is a wealth of kinetic and functional data for 5c.c7 interactions with the moth cytochrome-*c*-derived agonist peptide (MCC 88-103) presented within the mouse MHCII I-E^k (dissociation constant [K_D] reported at 22.9–43.5 μM), the weak agonist T102S peptide (K_D = 206 μM; ~4-fold lower potency), and the immeasurably weak antagonist T102G peptide (Corse et al., 2010; Gottschalk et al., 2010; Huppa et al., 2010).

Prior to testing the models, we functionally characterized CD4. *In vitro* 5c.c7$^+$ CD4$^+$ T cell responses mirror their *in vivo* responses to MCC and T102S (Corse et al., 2010), so we stimulated naive transgenic (Tg) 5c.c7$^+$ CD4$^+$ T cells with MCC, T102S, or T102G in the presence of anti-CD8 (control) or anti-CD4 monoclonal antibodies (mAb) *in vitro*. I-E^{k+} M12 cells were used as APCs for consistency with subsequent experiments (Figure S1B). Anti-CD4 reduced responses to MCC and eliminated responses to T102S, while no responses were observed to T102G (Figure 1A). We also evaluated CD69 expression and apoptosis of 5c.c7$^+$ CD4$^+$ CD8$^-$ Tg thymocytes *in vitro* as they are more sensitive to low-affinity ligands. Anti-CD4 reduced responses to T102S as well as T102G (Figures 1B, S1C, and S1D). Moving to more reductionist systems, we evaluated interleukin-2 (IL-2) production by 5c.c7$^+$ CD4$^+$ or CD8α^+ 58$\alpha^-\beta^-$ T cell hybridomas. Anti-CD4 eliminated responses to MCC and T102S for CD4$^+$ cells, while CD8$^+$ (no CD4) cells did not respond (Figure 1C). These data show that CD4 increases signaling by the 5c.c7 TCR in primary cells and T cell hybridomas responding to agonist and weak pMHCII.

Since the frequency of CD4:Lck association influences TCR signaling (Stepanek et al., 2014), we also asked how a CD4-Lck fusion influences the perceived potency of MCC, T102S, and T102G. Previously, we reported that 5c.c7$^+$ CD4-Lck$^+$ 58$\alpha^-\beta^-$ cells make IL-2 in response to M12 cells expressing tethered pMHCII with an unexpected hierarchy of T102G > T102S > MCC and also respond to null peptides in a manner that depended on high levels of pMHCII (Parrish et al., 2016). Here, analysis of IL-2 production in response to a peptide titration showed the proper hierarchy of potency (MCC > T102S > T102G), but T102G elicited a greater response than T102S and MCC at the highest peptide concentration (Figure 1D). A small amount of IL-2 was also produced without exogenous peptides, consistent with intrinsic TCR scanning of MHCII (Parrish et al., 2016). Expression of a CD4-Lck mutated in the D1 domain (CD4T$^{\Delta bind}$-Lck), where crystal structures show CD4-MHCII interactions and which impairs an ordered spatial relationship between CD4 and the TCR-CD3 subunits upon TCR engagement (Glassman et al., 2016; Wang et al., 2001a), did not facilitate IL-2 production to any of the peptides, so overexpression of Lck did not account for our results.

Since CD4:Lck interactions are not essential for CD4 function, we also interrogated how CD4-MHCII interactions impact TCR signaling in the absence of direct CD4:Lck interactions (Killeen and Littman, 1993; Parrish et al., 2016). We used C-terminally truncated CD4 (CD4T), which lacks the cysteine clasp that mediates CD4:Lck interactions but nevertheless enhances IL-2 production by 5c.c7$^+$CD4T$^+$ 58$\alpha^-\beta^-$ T cell hybridomas to ~60%–80% of levels observed with cells expressing full-length CD4, depending on the pMHCII density, and >10-fold relative to cells lacking CD4 (Parrish et al., 2015, 2016). With CD4T, intracellular Lck is available to phosphorylate ITAMs but cannot directly tether CD4 to a TCR-CD3-pMHC unit via interactions with the CD3ε proline rich sequence (PRS), the CD3ε basic rich sequence (BRS), or with phosphorylated ITAMs via its SH2 domain (Li et al., 2017; Mingueneau et al., 2008; Xu and Littman, 1993). CD4T was required for IL-2 production in response to MCC and T102S, when compared with CD4T$^{\Delta bind}$ (Figure 1E). CD4-MHCII interactions via the D1 domain thus impact the

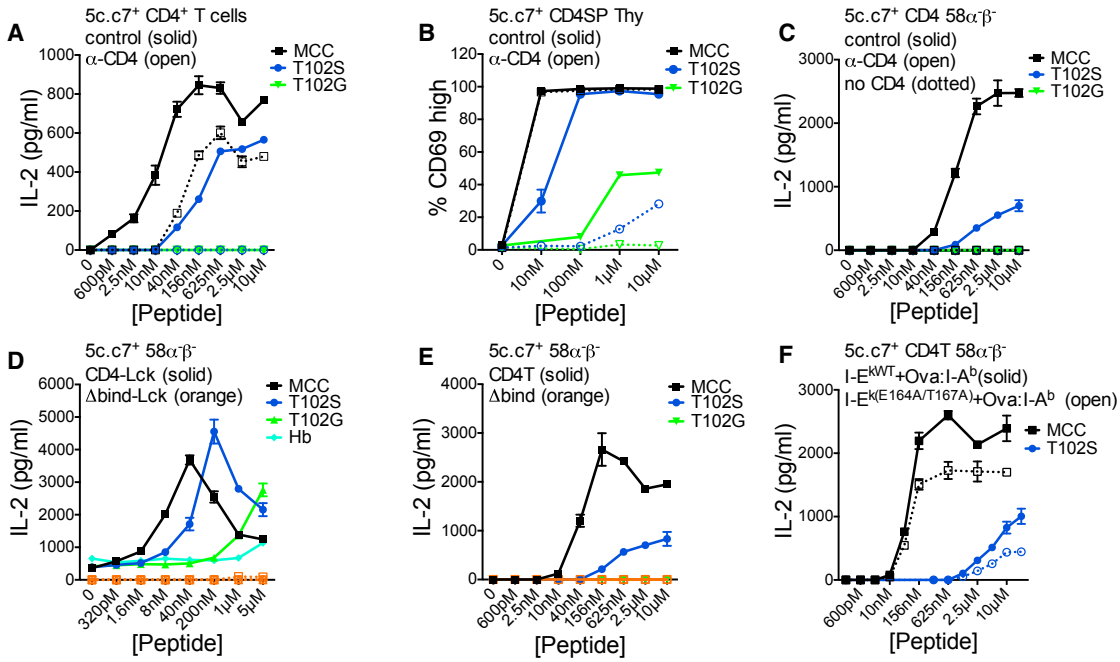

Figure 1. CD4 Enhances TCR-CD3 Signaling

(A) IL-2 production by CD4$^+$ T cells from 5c.c7 TCR Tg mice cultured with I-E^{k+} M12 cells, peptide, and control (α-CD8) or α-CD4 mAb.

(B) Percentage of CD69$^+$ 5c.c7 TCR Tg CD4$^+$CD8$^-$ (SP) thymocytes after 14-hr culture with I-E^{k+} M12 cells, peptide, and control (α-CD8) or α-CD4 mAb.

(C–E) IL-2 production by (C) 5c.c7$^+$ CD8α$^+$ (no CD4) or CD4$^+$ 58α$^-$β$^-$ cultured with I-E^{k+} M12 cells, peptide, and control or α-CD4 mAb; (D) 5c.c7$^+$ CD4-Lck$^+$ or CD4$^{\Delta bind}$-Lck$^+$ 58α$^-$β$^-$ cells cultured with I-E^{k+} M12 cells and peptide; (E) 5c.c7$^+$ 58α$^-$β$^-$ cells expressing CD4T or CD4T$^{\Delta bind}$.

(F) 5c.c7$^+$ CD4T$^+$ 58α$^-$β$^-$ cells cultured with Ova:I-A^b plus WT I-E^k or E164A+T167A mutant I-E^k M12 cells.

Data are mean ± SEM of triplicate wells. IL-2 was measured by ELISA at 16 hr. Results shown are representative of two or more independent experiments. See also Figure S1.

perceived potency of a pMHCII even when CD4 cannot directly interact with Lck.

Finally, we asked whether CD4T binds to the same pMHCII as the TCR to elicit IL-2 production, as indicated by previous studies of MHCI or MHCII mutants that impair CD8 or CD4 function, respectively (Connolly et al., 1990; Krogsgaard et al., 2005). M12 cells were transduced with I-E^k or an I-E$^{k.E164A+T167A}$ mutant that impairs CD4T function, along with tethered OVA:I-A^b that has an intact CD4 binding site but cannot present the MCC peptide (Figure S1E) (König et al., 1992; Krogsgaard et al., 2005). Consistent with prior results, the mutants impaired IL-2 production by 5c.c7$^+$CD4T$^+$ 58α$^-$β$^-$ T cell hybridomas in response to MCC and T102S, providing additional evidence that CD4T binds the same pMHCII as the TCR (Figure 1F).

CD4 Increases TCR-Mediated Cell Coupling

Functional T cell responses require coupling to APCs, so we used flow cytometry to evaluate CD4's role in meditating coupling of 5c.c7$^+$CD4T$^+$ or CD4T$^{\Delta bind}$ 58α$^-$β$^-$ cells to M12 cell expressing tethered pMHCII. 5c.c7$^+$ CD4T$^+$ 58α$^-$β$^-$ cells coupled to T102S:I-E^{k+} and T102G:I-E^{k+} M12 cells at a higher relative frequency than CD4T$^{\Delta bind}$ cells, and treatment with PP2 to inhibit kinase activity yielded similar results (Figures 2A, 2B, S2A, and S2B) (Bain et al., 2007).

To further investigate whether the TCR and CD4 mediate coupling on their own we tested (1) whether TCR-pMHCII interactions mediate cell coupling in the absence of signaling or other TCR engagement-associated events (e.g., Nck or Lck interactions with the CD3ε PRS or basic rich sequences) (Gil et al., 2002; Li et al., 2017; Mingueneau et al., 2008; Xu and Littman, 1993); and (2) whether CD4T contributes to cell coupling. The 5c.c7 TCR was expressed with truncated CD3 subunits (CD3T) that lack their intracellular domains, and either CD4T or CD4T$^{\Delta bind}$ on M12 cells, while our panel of tethered pMHCII were expressed on 58α$^-$β$^-$ cells (Figure S2C). Again, the frequency of couple formation followed the expected hierarchy (MCC > T102S > T102G > Hb). MCC-driven coupling was not increased by CD4T relative to CD4T$^{\Delta bind}$, and neither CD4T nor CD4T$^{\Delta bind}$ cells coupled to Hb APCs even with high expression of pMHCII (Figures 2C, S2C, and S2D). 5c.c7 interactions with T102S:I-E^k were sufficient to mediate coupling (CD4T$^{\Delta bind}$ cells) and CD4T increased these interactions (Huppa et al., 2010). Finally, the affinity of 5c.c7 for T102G:I-E^k was too weak to mediate cell coupling by CD4T$^{\Delta bind}$ cells, yet when combined with CD4-MHCII interactions cell coupling was achieved. These data show that CD4 can enhance cell coupling mediated by low-affinity TCR-pMHCII interactions at high pMHCII density.

To test whether CD4T impacts coupling with different TCR-pMHCII pairings, we used the 2B4, B3K506, and B3K508 TCRs in the same experimental setup. 2B4 is unique as it lacks five of the eight features typical of cytochrome-reactive TCRs, like 5c.c7, has higher affinity for MCC and T102S (K_D ≈5.5–8.7

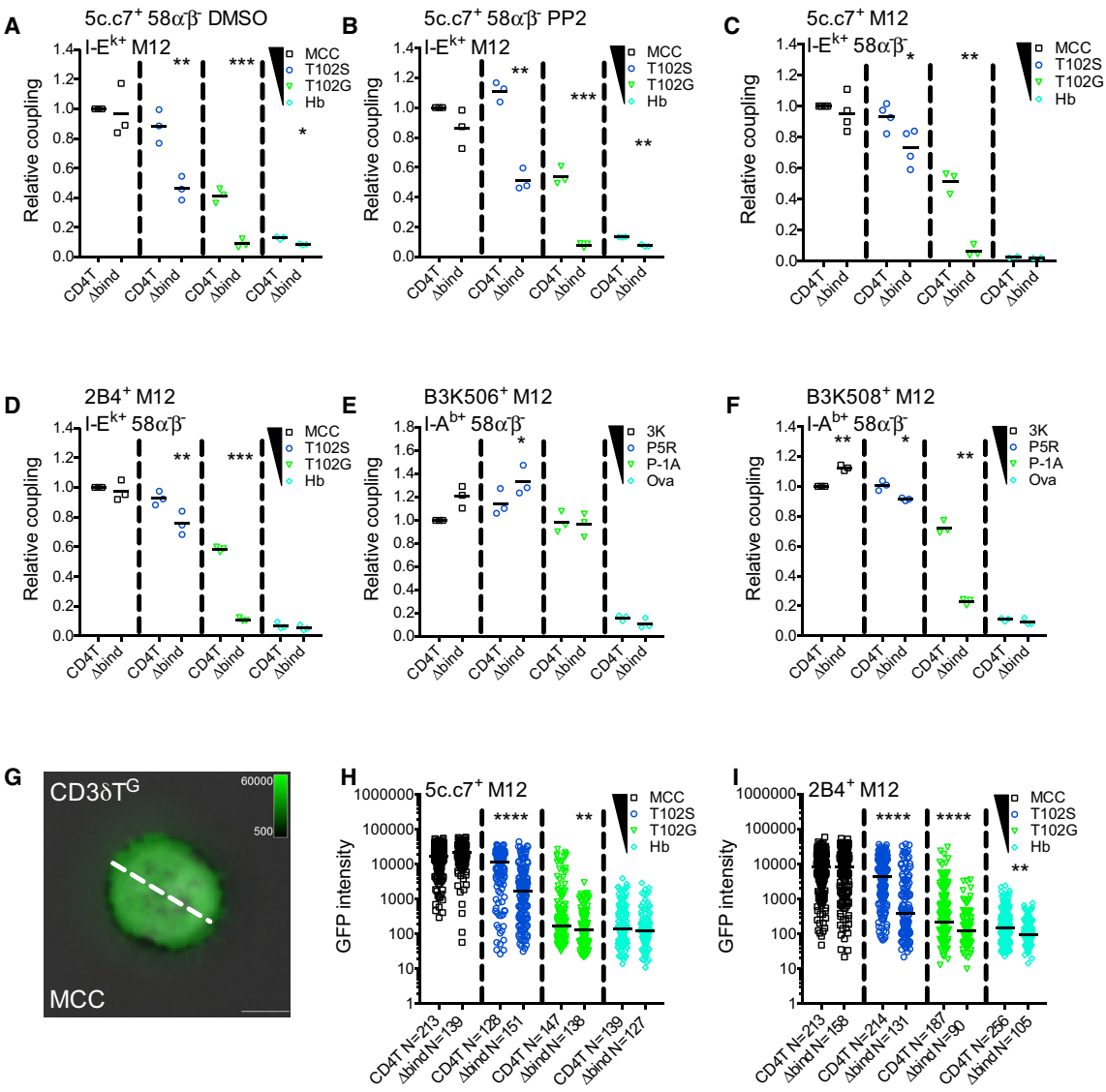

Figure 2. CD4 Enhances Cell Couple Formation and TCR Accumulation

(A and B) Relative cell coupling between 5c.c7$^+$ CD4T$^+$ or CD4T$^{\Delta bind+}$ 58$\alpha^-\beta^-$ cells cultured with the indicated tethered pMHCII$^+$ M12 cells in the presence of (A) DMSO as a vehicle control or (B) PP2 to inhibit kinase activity.

(C–F) CD3T$^+$ CD4T$^+$ or CD4T$^{\Delta bind+}$ M12 cells expressing the (C) 5c.c7 TCR, (D) 2B4 TCR, (E) B3K506 TCR, or (F) B3K508 TCR were cultured with 58$\alpha^-\beta^-$ cells expressing the indicated tethered pMHCII.

Cell coupling is shown relative to the couple frequency observed in the CD4T MCC condition for (A)–(D) or the CD4T 3K condition for (E) and (F). Each data point represents an individual experiment (3–4 experiments per condition); bars represent mean. Data were analyzed using a paired Student's t test (*$p < 0.05$, **$p < 0.01$, ***$p < 0.001$). See also Figure S2.

(G) Representative TIRFM image showing CD3δT^G accumulation on a MCC:I-E^k-coated surface (pseudocolored green) overlayed on a bright-field image. The dashed line represents the region of interest (ROI) exported for analysis. Scale bars represent 5 μm and look up tables indicate mEGFP intensity units.

(H and I) TCR-CD3 complex accumulation. Each dot represents GFP intensity of a single cell for (H) CD3δT^G or (I) 2B4β^G on immobile pMHCII surfaces with the indicated peptides. n = total number of analyzed cells per condition. Data were tested for normality using a D'Agostino and Pearson omnibus normality test followed by a Mann-Whitney test (*$p < 0.05$, **$p < 0.01$, ***$p < 0.001$, ****$p < 0.0001$). Results shown are representative of two experiments.

and 33.8–90 μM, respectively) and drives distinct effector differentiation (Fazilleau et al., 2009; Krogsgaard et al., 2003; Newell et al., 2011; Wu et al., 2002). CD4T increased 2B4-mediated coupling to T102S, and more so to T102G, but not to MCC (Figure 2D), indicating again that CD4 contributes to coupling when TCR-pMHCII affinity falls below some threshold (>33–90 μM). The B3K506 TCR binds the 3K, P5R, and P-1A peptide in I-A^b with affinities above this mark (K_D = 7, 11, and 26 μM, respectively), while the B3K508 TCR binds the same pMHCII with a broader range of affinities (29, 93, and >550 μM, respectively), allowing us to further test this idea (Govern et al., 2010). CD4T did not increase cell coupling driven by B3K506 for any peptides

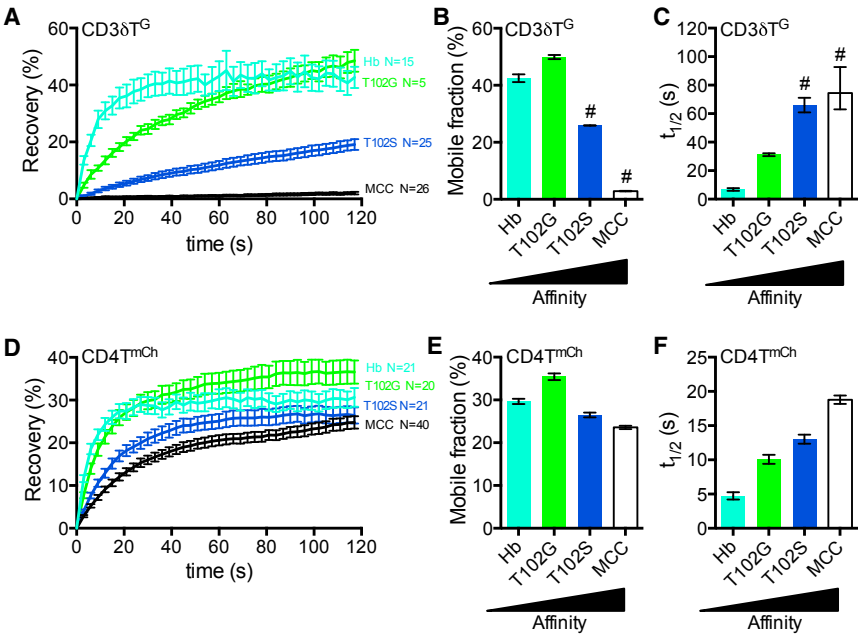

Figure 3. TCR-CD3 and CD4 Mobility Decrease as TCR-pMHCII Affinity Increases

(A–C) FRAP analysis of CD3δT^G for 5c.c7$^+$ CD3T$^+$ CD4T$^+$ M12 cells. Images were collected for 2-min postbleach at 3-s intervals. (A) Recovery trace represents mean ± SEM for the indicated number (n) of cells. (B) Mobile fraction (%) and (C) half-life ($t_{1/2}$) for recovery were determined by curve fitting. Error bars indicate 95% confidence interval.

(D–F) FRAP of CD4T^{mCh}. (D) Recovery trace, (E) mobile fraction (%) and (F) half-life ($t_{1/2}$) as presented in (A)–(C).

# denotes values with poor fitting with an exponential function. Results shown are representative of at least two experiments. See also Figure S3.

but increased B3K508-mediated coupling to P5R and P-1A (Figures 2E, 2F, and S2E); further demonstrating that CD4 can contribute to cell coupling for lower-affinity TCR-pMHCII interactions.

These results could reflect an additive contribution to adhesion if CD4 and the TCR bind pMHCII independently in a V-like arch, although a CD4-MHCII K_D >2.5 mM makes this remote. Alternatively, they could reflect a cooperative effect similar to that described for some cytokine receptors and expected in a compact macrocomplex (Spangler et al., 2015).

CD4 Increases TCR Adhesion to pMHCII *In Situ*

To further analyze CD4's impact on TCR-pMHCII interactions, we asked whether CD4T increased TCR-CD3T^G accumulation on glass coverslips coated with pMHCII monomers relative to CD4T$^{\Delta bind}$ (Glassman et al., 2016). Bright-field microscopy of 5c.c7$^+$CD3T$^+$CD4T$^+$ M12 cells allowed an unbiased survey of all cells in the field, while TCR-CD3T^G intensity was measured by live total internal reflection fluorescence microscopy (TIRFM) for a region of interest (ROI) across the widest point of contact (Figure 2G). CD4T$^{\Delta bind}$ was used instead of anti-CD4 since prior studies of 5c.c7-MCC:I-E^k interactions *in situ* reported a slight decline in TCR dwell time with anti-CD4, and one reported a reduction in the total number of TCR-pMHC interactions per cell that was attributed to interference from the antibody (Huppa et al., 2010; O'Donoghue et al., 2013).

Both 5c.c7$^+$CD3T$^+$CD4T$^+$ and CD4T$^{\Delta bind+}$ cells had TCR-CD3T^G intensity that was proportional to the affinity of TCR-pMHCII interactions (MCC > T102S > T102G > Hb) (Figure 2H). But CD4T dramatically enhanced the intensity on the T102S and T102G surfaces compared to CD4T$^{\Delta bind}$. These data indicate that CD4-MHCII interactions enhance weak TCR-pMHCII interactions. Similar results were observed with 2B4$^+$CD3T$^+$CD4T$^+$ and CD4T$^{\Delta bind+}$ M12 cells (Figure 2I).

CD4 Mobility on pMHCII Surfaces Is Proportional to TCR-pMHCII Affinity and Density

We next used fluorescence recovery after photobleaching (FRAP) to analyze TCR-CD3 and CD4 dwell time on pMHCII *in situ* in order to test predictions of the relevant models (Figures S3A and S3B). For example, TCR-pMHCII affinity should not influence independent CD4-MHCII interactions in a V-like arch but should in a compact macrocomplex where TCR-CD3 and CD4 interact around a nucleating pMHCII. TCR$^+$CD3T$^+$CD4T$^+$ or CD4T$^{\Delta bind+}$ M12 cells were used to test these predictions in the absence of downstream events associated with TCR engagement.

To establish the system, we calculated the mobile fraction and $t_{1/2}$ of recovery of 5c.c7-CD3T^G molecules as they exchanged in and out of a bleached ROI on cells bound to surfaces coated with pMHCII of increasing affinity (Figures 3A–3C; Movies S1 and S2) (Klammt et al., 2015). This movement would be a measure of on and off rates as well as surface mobility. Surface plasmon resonance (SPR) cannot detect 5c.c7 interactions with T102G:I-E^k, but FRAP showed an increase in TCR-CD3T^G $t_{1/2}$ on the T102G surfaces compared with Hb surfaces that increased further on the T102S and MCC surfaces. The near lack of mobility observed on MCC surfaces showed that rebinding impacts TCR-CD3T^G confinement in the bleached area as the $t_{1/2}$ for a 5c.c7 TCR bound to MCC:I-E^k at 37°C is 2.28 s (Huppa et al., 2010). These data establish that TCR-CD3T^G dwell time measured by FRAP follows the expected hierarchy.

Next, we asked whether TCR-pMHCII affinity does or does not impact CD4T mobility *in situ*, as predicted by the compact or V-like macrocomplex models, respectively (Figures 3D–3F). While the mobile fraction was minimally impacted by changes in TCR-pMHCII affinity, the CD4T^{mCh} $t_{1/2}$ increased proportionally to the affinity of TCR-pMHCII interactions on 5c.c7$^+$CD3T$^+$CD4T$^+$ M12 cells. Similar results were obtained with the 2B4$^+$CD3T$^+$CD4T$^+$ M12 cells, although CD4T mobility was not slowed by MCC to a greater extent than T102S (Figures S3C–S3E).

To determine whether the observed differences in CD4T $t_{1/2}$ were due to direct interactions versus TCR-CD3 crowding, we

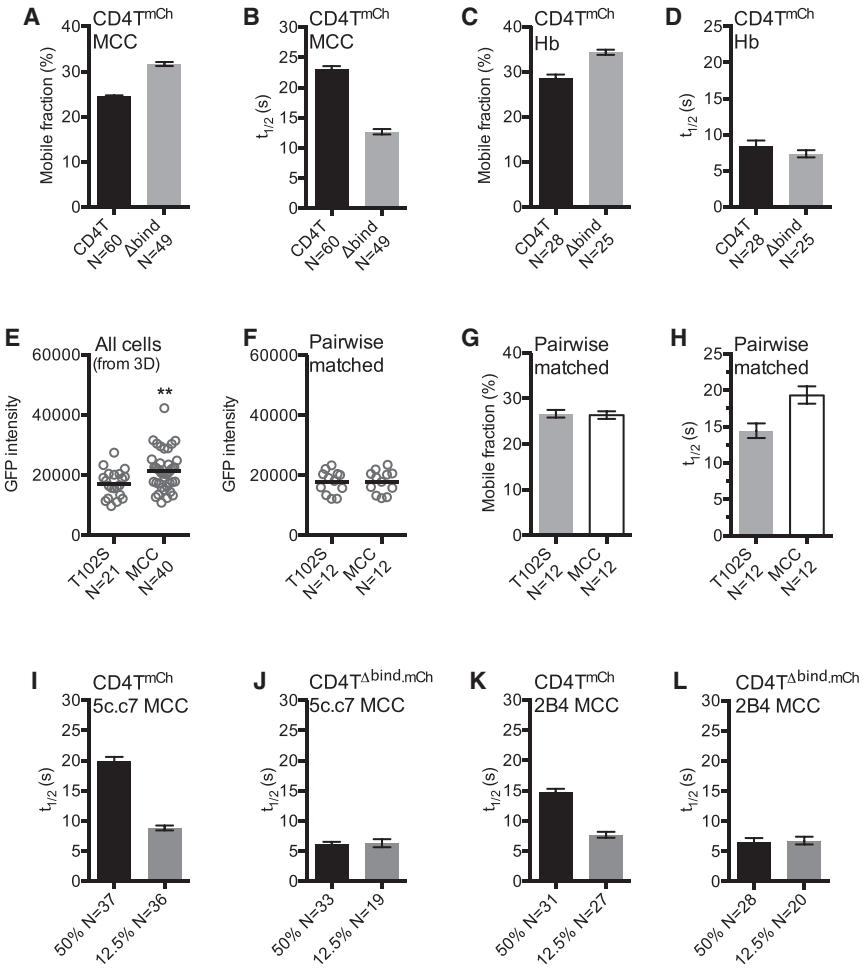

Figure 4. CD4 Dwell Time Depends upon TCR Engagement

(A–D) 5c.c7^{+} CD4T^{mCh+} or CD4T$^{\Delta bind.\ mCh+}$ M12 cells were adhered to (A and B) MCC:I-E^{k} or (C and D) Hb:I-E^{k}-coated surfaces for mCh FRAP analysis as in Figures 3E and 3F.

(E) mEGFP intensity of cells from Figure 3D on T102S or MCC surfaces. Values are post-mCherry bleaching to account for differences in intensity due to CD3δT^{G}::CD4T^{mCh} FRET (Glassman et al., 2016).

(F) mEGFP intensity of pairwise mEGFP intensity-matched cells (<5% variance) from (E).

(G and H) Mobile fraction (G) and mCh $t_{1/2}$ (H) of pairwise mEGFP-matched cells from (F).

(I–L) mCh $t_{1/2}$ for TCR^{+} CD4T^{mCh+} or CD4T$^{\Delta bind.\ mCh+}$ M12 cells expressing the (I and J) 5c.c7 or (K and L) 2B4 TCR adhered to surfaces coated with 50% or 12.5% MCC:I-E^{k} diluted in Hb:I-E^{k}.

Data in (E) and (F) are presented as mean and analyzed by t test (**p < 0.01). n = number of cells analyzed per condition. Error bars for FRAP indicate 95% confidence interval. Results shown are representative of at least two experiments. See also Figure S4.

compared CD4T^{mCh} and CD4T$^{\Delta bind.mCh}$ mobility on 5c.c7 cells adhered to MCC:I-E^{k} where CD4T did not increase TCR-CD3T^{G} intensity (Figure 2H). CD4T$^{\Delta bind.mCh}$ recovered more rapidly than CD4T^{mCh}, and CD4T^{mCh} intensity increased more than CD4T$^{\Delta bind.mCh}$ (Figures 4A, 4B, and S4A–S4C). On Hb:I-E^{k}, where TCR-CD3T^{G} and CD4T^{mCh} versus CD4T$^{\Delta bind.mCh}$ intensity were equivalent, we observed a small difference in mobile fraction but not $t_{1/2}$ (Figures 4C, 4D, and S4D–S4F). We also pairwise-matched 5c.c7 cells with TCR-CD3T^{G} intensities that varied by less than 5% on T102S and MCC to compare CD4T dwell times under conditions of equivalent TCR-CD3 crowding and intact CD4-MHCII interactions (Figures 4E and 4F). Here, the CD4T^{mCh} $t_{1/2}$ was longer on the MCC surface than the T102S surface, while the mobile fraction was equivalent, indicating that TCR-pMHCII dwell time impacts CD4T-pMHCII dwell time (Figures 4G, 4H, and S4G). CD4T mobility is therefore sensitive to TCR-pMHCII interactions.

Finally, if TCR and CD4 bind pMHCII independently in a V-like arch, then CD4 $t_{1/2}$ should not be impacted by the quality of peptides presented therein, but the peptide sequence would impact the CD4 $t_{1/2}$ in a compact macrocomplex. For 5c.c7 cells, a decrease in CD4T^{mCh} $t_{1/2}$ was observed on surfaces in which MCC:I-E^{k} was diluted from 50% to 12.5% to 4% into Hb:I-E^{k} that was not mirrored by CD4T$^{\Delta bind.mCh}$ $t_{1/2}$ on such surfaces (Figures 4I, 4J, and S4H–S4J). The most dramatic difference was observed from 50% to 12.5% MCC:I-E^{k}, so we tested 2B4 cells under these conditions and obtained similar results (Figures 4K, 4L, S4K, and S4L). These data further establish that TCR engagement impacts CD4 dwell time.

TCR-CD3 Mobility on pMHCII Surfaces Is Impeded by CD4-MHCII Interactions

We next asked whether CD4-MHCII interactions impact TCR-CD3 dwell time by measuring TCR-CD3T^{G} mobility on TCR^{+}CD3T^{+}CD4T^{+} or CD4T$^{\Delta bind+}$ M12 cells. CD4T minimally impacted TCR-CD3T^{G} recovery on MCC surfaces, compared with CD4T$^{\Delta bind}$, for either 5c.c7 or 2B4 cells (Figures S5A and S5B). As our initial analysis suggested that TCR rebinding on the high density MCC surface impeded TCR-CD3T^{G} mobility, we also analyzed TCR-CD3T^{G} mobility on surfaces with 12.5% MCC:I-E^{k} diluted into Hb:I-E^{k}. Here, the presence of CD4T slightly reduced the mobile fraction but dramatically increased the TCR-CD3T^{G} $t_{1/2}$ compared to CD4T$^{\Delta bind}$ for both the 5c.c7 and 2B4 TCRs (Figures 5A–5D, S5C, and S5D), showing the CD4T can increase TCR dwell time on low ligand densities of agonist pMHCII. To ask whether CD4T impacts TCR dwell times on lower-affinity ligands we monitored TCR-CD3T^{G} mobility on T102S surfaces. Again, CD4T reduced the mobile fraction and increased TCR-CD3T^{G} $t_{1/2}$ compared

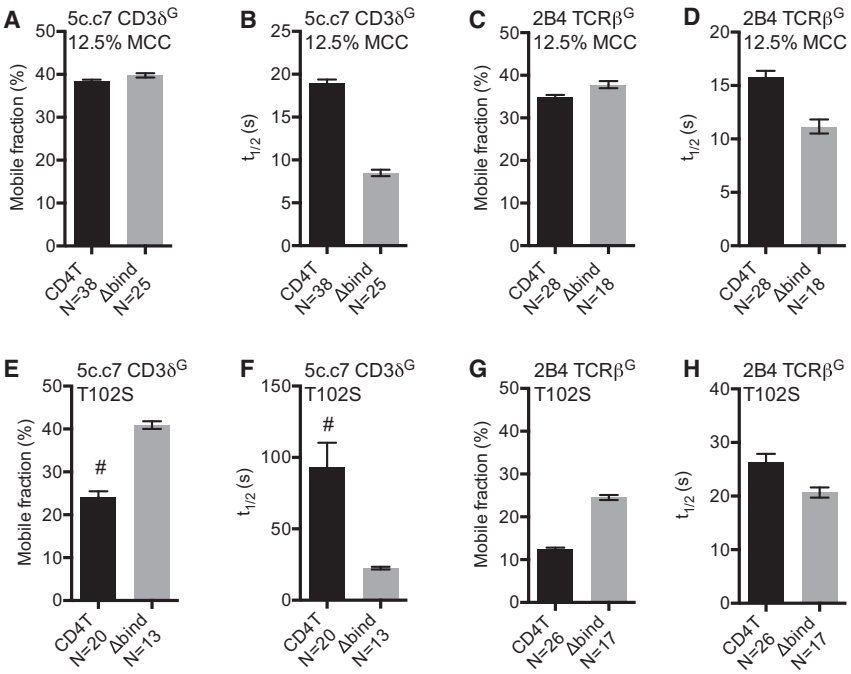

Figure 5. CD4 Increases TCR-CD3 Confinement on pMHCII

FRAP of TCR-CD3T^G complexes for TCR$^+$ CD4T$^+$ or CD4T$^{\Delta bind+}$ M12 cells.

(A–D) FRAP of TCR-CD3T^G on surfaces coated with 12.5% MCC:I-E^k in Hb:I-E^k. (A) Mobile fraction (%) and (B) half-life ($t_{1/2}$) for 5c.c7 TCR + CD3δT^G. (C) Mobile fraction (%) and (D) half-life ($t_{1/2}$) for 2B4 TCR (2B4β^{G+}).

(E–H) FRAP of TCR-CD3T^G on T102S:I-E^k-coated surfaces. (E) Mobile fraction (%) and (F) half-life ($t_{1/2}$) for 5c.c7 TCR + CD3δT^G. (G) Mobile fraction (%) and (H) half-life ($t_{1/2}$) for 2B4 TCR (2B4β^{G+}).

n = number of cells analyzed per condition. Error bars are 95% confidence interval. Results shown are representative of at least three experiments. See also Figure S5.

to CD4T$^{\Delta bind}$ for both the 5c.c7 and 2B4 TCRs (Figures 5E–5H, S5E, and S5F). These data are most consistent with a compact macrocomplex.

Mutations in the CD4 D3 Domain Impair Function

A final difference between the V-like and compact macrocomplex models is that the former dictates that CD4 only binds MHCII via the D1 domain, while the latter predicts that CD4 contacts the TCR-CD3-pMHCII axis along its length. Our CD4$^{\Delta bind}$ mutant provides evidence for the importance of the D1 domain, but to further test these models required mutants in an MHCII-distal region of CD4.

Prior studies proposed that the D3 domain surface interacts with the TCR-CD3 complex, as mutating F208 and F227 (using UniProt convention) that extend into the CD4 D3 domain hydrophobic core impair signaling (Figure S6A) (Vignali and Vignali, 1999). Since the cavity created by F208A and F227A could destabilize the D3 domain surface, we examined the surface above F208 and F227 and found that P228 and F231, as well as P281 on an adjacent loop, constitute a conserved nonpolar patch that borders a hydrophobic pocket (Figures S6A and S6B). Such patches can mediate protein:protein interactions (DeLano et al., 2000), leading us to ask whether changing the nature of this surface by mutagenesis (CD4T$^{P228E+F231E}$ and CD4T^{P281E}) would reduce its contribution to TCR signaling, proximity to the TCR-CD3 complex, and CD4 mobility upon pMHCII engagement. Glutamate was used to impart a negative charge on this surface, while mutating the rigid prolines was also likely to impact the shape, mobility, or surface stability (Wang et al., 2009). Indeed, for P281 that facilitates a turn on one side of the nonpolar patch, the CD4T^{P281E} mutant had slightly reduced cell-surface expression and increased CD4T^{P281E}::CD4T^{P281E} Förster resonance energy transfer (FRET) compared with the WT or CD4T$^{P228E+F231E}$ mutant, which may indicate instability and increased aggregation (Figures S6C–S6E).

58α$^-$β$^-$ cell lines expressing the 5c.c7 TCR and wild-type or mutant CD4T molecules were generated to assess the functional impact of these mutations. CD4T$^{P228E+F231E}$ cells had reduced IL-2 production, TCR downregulation, and CD69 expression in response to tethered MCC:I-E^k, T102S:I-E^k, or T102G:I-E^k pMHCII expressed on M12 cells compared with CD4T cells (Figures 6A–6C). After sorting CD4T and CD4T^{P281E} cells for matched surface expression (Figure S6F), CD4T^{P281E} cells also made less IL-2 upon TCR engagement than the CD4T cells (Figure 6D). Since sorting requires coating cells with mAbs to CD4, which could deliver a signal and impact the responsiveness of cells that expanded thereafter, we used unsorted cells for our analysis of TCR downregulation and CD69 expression as flow cytometry allowed us to directly compare matched subsets by gating on equivalent CD4 expression (Figure S6G). Here, again we observed reduced responses by the CD4T^{P281E} cells relative to the CD4T cells for multiple independently generated sets of lines (Figures 6E and 6F).

As a final functional assay, we made 5c.c7$^+$ 58α$^-$β$^-$ cells expressing a CD4-Lck fusion, CD4T$^{P228E+F231E}$-Lck, or CD4$^{\Delta bind}$-Lck since we have reported that 5c.c7$^+$ CD4-Lck$^+$ 58α$^-$β$^-$ cells make IL-2 in response to high expression levels of MHCII presenting "shaved" peptides with alanine substitutions in the TCR contact residues (Parrish et al., 2016). Our prior data suggest that the TCR and CD4 constantly work together to scan the peptide content of MHCII, so we reasoned that the CD4$^{P228E+F231E}$ should have a profound impact on TCR scanning if the macrocomplex model has merit. Indeed, for CD4-Lck and CD4$^{P228E+F231E}$-Lck cells with equivalent expression, the mutation nearly ablated IL-2 production in response to the shaved MCC4A peptide in I-E^k or the shaved 2W4A peptide in I-A^b, while the CD4$^{\Delta bind}$-Lck cells had no response (Figures 6G, 6H, and S6H).

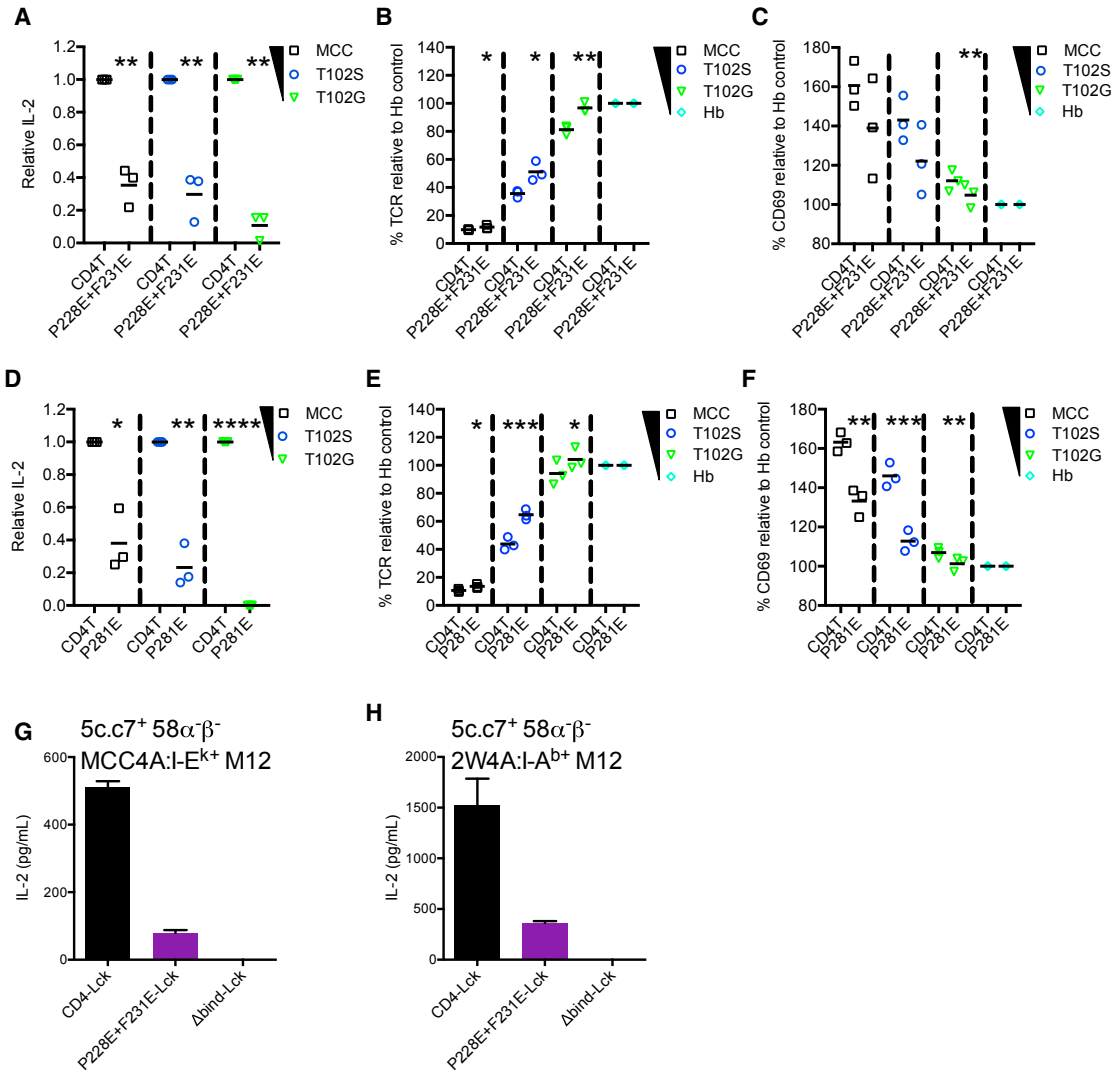

Figure 6. The CD4 D3 Domain Contributes to TCR-CD3 Signaling

(A–C) 5c.c7^{+} CD4T^{+} or CD4T$^{P228E+F231E+}$ 58α^{-}β^{-} cells were cultured with M12 cells expressing tethered pMHCII for 16 hr. (A) Relative IL-2 production, (B) TCR downregulation, and (C) CD69 upregulation were assessed. Each data point represents an experiment with an independently generated cell line. Bars represent mean.

(D–F) 5c.c7^{+} CD4T^{+} or CD4T^{P281E+} 58α^{-}β^{-} cells were cultured with M12 cells expressing tethered pMHCII for 16 hr. (D) Relative IL-2 production for fluorescence-activated cell sorted (FACS) CD4T and CD4T^{P281E} cells. Each point represents an independent experiment from one set of sorted cell lines. Bars represent mean. (E) TCR downregulation and (F) CD69 upregulation were assessed on unsorted cells that were CD4 expression-matched by flow cytometry. Each point represents an experiment with an independently generated cell line. Bars represent mean.

Relative IL-2 values were normalized to CD4T controls for each condition. CD69 upregulation and TCR downregulation data are presented relative to the Hb condition for each cell line. Data in (A)–(F) were from 3 experiments and analyzed using a paired Student's t test (*$p < 0.05$, **$p < 0.01$, ***$p < 0.001$).

(G and H) 5c.c7^{+} CD4-Lck^{+}, CD4$^{P228E+F231E}$-Lck^{+}, or CD4T$^{\Delta bind}$-Lck^{+} 58α^{-}β^{-} cells were cultured with M12 cells expressing (G) MCC4A:I-E^{k} or (H) 2W4A:I-A^{b} for 16 hr.

IL-2 was measured by ELISA. Data are mean ± SEM of triplicate wells. Results shown are representative of four independent experiments. See also Figure S6.

D3 Domain Mutants Impair the Formation and Stability of the Macrocomplex

Next we asked whether the CD4T$^{P228E+F231E}$ and CD4T^{P281E} mutants impact TCR-CD3 accumulation on immobile T102S: I-E^{k} surfaces. Both the CD4T$^{P228E+F231E}$ and CD4T^{P281E} cells had reduced CD3δT^{G} intensity compared to CD4T cells (Figure 7A).

Since CD4 is closer to the CD3 subunits than predicted by a V-like arch (Glassman et al., 2016), we also used donor recovery after acceptor photobleaching to calculate the efficiency of FRET$_{E}$ between CD3δT^{G} and CD4T^{mCh}, CD4T$^{P228E+F231E.mCh}$ or CD4T$^{P281E.mCh}$. M12 cells expressing the 5c.c7 TCR, CD3T subunits (including CD3δT^{G}), and CD4T^{mCh} or the mutants were used to reduce our analysis to interactions mediated by the

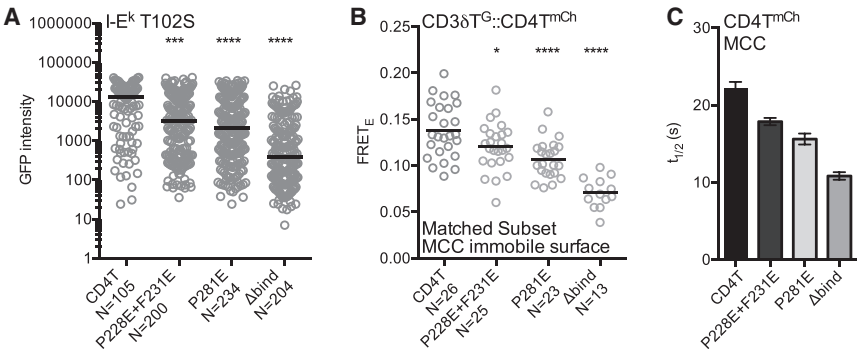

Figure 7. Mutations in the CD4 D3 Domain Impact Macrocomplex Assembly and Stability

(A–C) 5c.c7$^+$ CD3T$^+$ CD4T$^+$, CD4T$^{P228E+F231E+}$, CD4T^{P281E+}, or CD4T$^{\Delta bind+}$ M12 cells were analyzed for (A) CD3δT^G intensity on T102S:I-E^k-coated surfaces in TIRF as in Figure 2, (B) CD3δT^G::CD4T^{mCh} FRET$_E$ on immobile MCC:I-E^k surfaces, and (C) FRAP of the indicated CD4T molecules adhered to MCC:I-E^k-coated surfaces as in Figure 3. Each dot represents an individual cell; black bars represent the mean value. n = number of cells analyzed per condition. Intensity and FRET$_E$ data were assessed for normality using a D'Agostino and Pearson omnibus normality test followed by a one-way analysis of variance (ANOVA) and Dunnet's multiple comparison test (*$p < 0.05$, ****$p < 0.0001$). Results shown are representative of at least two experiments. See also Figure S7.

ectodomains of CD4 and the TCR-CD3 complex *in situ* in the absence of signaling or other TCR engagement-associated events. Immobile MCC:I-E^k surfaces were used to maximize the formation of putative CD4 docking sites along the TCR-CD3-pMHC axis (Figures S7A and S7B). The lower level of CD4T^{P281E} expression compared with CD4T or CD4T$^{P228E+F231E}$ cells was accounted for by analyzing subsets of cells matched for the intensity of CD3δT^G and CD4T^{mCh} (Figures S7D–S7G), as described previously (Glassman et al., 2016). Without pMHCII, CD3δT^G::CD4T^{mCh} FRET$_E$ was indistinguishable between the cell lines (Figure S7C), but on immobile MCC surfaces the CD4T$^{P228E+F231E}$, CD4T^{P281E} and CD4T$^{\Delta bind}$ cells showed reductions in FRET$_E$ compared with the CD4T cells (Figure 7B). The CD4T$^{P228E+F231E}$ cells indicate that the D3 domain is important for increasing the frequency of CD4 and TCR-CD3 complexes that come into close association upon interactions with agonist pMHCII. The CD4T^{P281E} cells support this conclusion, although their tendency to aggregate (Figure S6C) means that fewer CD4T^{P281E} molecules may be available to interact with the TCR-CD3 complex.

Finally, we used FRAP to determine how the CD4 mutants impact the kinetics of macrocomplex formation on immobile MCC:I-E^k surfaces since the higher-affinity TCR-pMHCII interactions should provide the highest resolving power. While the D3 domain mutations did not impact the mobile fraction, the hierarchy of $t_{1/2}$ (CD4T > CD4T$^{P228E+F231E}$ > CD4T^{P281E} > CD4T$^{\Delta bind}$) mirrored the FRET$_E$ results (Figures 7C, S7H, and S7I).

These data further indicate that the D3 domain of CD4 is involved in the formation and stabilization of the TCR-CD3-pMHC-CD4 macrocomplex, albeit the same caveat holds for the CD4T^{P281E} result here as above. Whether the CD4T$^{P228E+F231E}$ mutations disrupted interactions between CD4 and the TCR-CD3-pMHC axis mediated by the native residues, or induced allosteric changes in residues that mediate interactions cannot be known from the data provided here. The D3 hydrophobic core was not altered, so any allosteric changes should be localized to adjacent residues rather than propagated to a distant site. Altogether, the results suggest that the conserved nonpolar patch or proximal residues are involved in macrocomplex assembly and function.

DISCUSSION

CD4 has long been enigmatic. Originally, it was viewed as an accessory molecule until antibody-crosslinking experiments were interpreted to mean that the TCR and CD4 physically interact; the term coreceptor was then offered to define CD4 as a component of a multi-subunit receptor complex for pMHCII in order to distinguish it from a subsidiary function such as adhesion (Janeway, 1988). Mutagenesis data were subsequently taken as evidence for TCR-CD4 interactions (Vignali et al., 1996; Vignali and Vignali, 1999). However, the V-like crystal structures altered this thinking since the TCR and CD4 would not directly interact (Wang et al., 2001a; Yin et al., 2012). A model that could reconcile these discordant results was proposed whereby the TCR-CD3 complex pre-associates with the CD4 D3 and D4 domains and crosslinks one TCR-pMHCII assembly to another (Irvine et al., 2002; Krogsgaard et al., 2005). But recent FRET and super-resolution data show that the TCR-CD3 complex and CD4 do not pre-associate in the absence of coincident pMHCII engagement or adopt the spatial relationship predicted by that model (Glassman et al., 2016; Roh et al., 2015). Thus, fundamental questions persist regarding how CD4 fits and works within this multi-subunit molecular machine.

The data presented here do not conform with expectations regarding how the TCR and CD4 should behave if they were to bind pMHCII in a V-like arch, but they are consistent with pMHCII receptor signaling having converged on a mechanism akin to cytokine signaling (Kuhns and Badgandi, 2012; Madrenas et al., 1997). For example, binding of the cytokine-specific IL-4Rα subunit to IL-4 forms a composite docking interface to which the degenerate γc subunit binds with a higher affinity than to IL-4 alone; only then are the IL-4Rα and γc-associated Janus Kinases positioned in a spatial and temporal relationship that facilitates signaling (Wang et al., 2009). By analogy, our data are consistent with the TCR-CD3 complex serving as a specific receptor subunit for pMHCII, while CD4 represents a degenerate subunit with no appreciable affinity for pMHCII on its own. In this scenario, the constrained docking polarity observed for TCRs on pMHCII (Rossjohn et al., 2015) results in a highly reproducible composite surface along the TCR-CD3-pMHCII axis to which CD4 would bind with higher affinity than to MHCII alone.

Docking would then position Lck in the proper spatial and temporal relationship with the CD3 ITAMs to allow for phosphorylation.

The most straightforward extracellular docking topology would follow an apparent shape complementarity between CD4 and the TCR-CD3-pMHCII axis (Figure S1A) since (1) structural data indicate that large-scale conformational changes in the TCR or CD3 ectodomains do not occur upon pMHCII or mitogenic mAb engagement; (2) experimental data point to a stable TCR-CD3 unit bound by continuous interactions between the ecto and transmembrane domains; and (3) FRET analysis indicate that CD4 is proximal to CD3δ (Call et al., 2002; Ding et al., 1999; Fernandes et al., 2012; Garcia et al., 1999; Glassman et al., 2016; Kuhns and Badgandi, 2012; Kuhns and Davis, 2007; Kuhns et al., 2010; Sun et al., 2001; Xu et al., 2006). An alternative hypothesis, akin to the permissive geometry model, is that TCR engagement moves the CD3 ectodomains to expose a CD4 contact site on the TCR (Minguet et al., 2007). Either way, initial CD4-MHCII interactions could allow a pivot from a V-like arch to a lower energy docked position via a ball-and-socket movement akin to the V_H-C_H elbow of antibodies (Lesk and Chothia, 1988). Or, docking may occur straight away. Importantly, once docked, an additional anchor could form via intracellular interactions between Lck and the CD3 subunits (Li et al., 2017; Mingueneau et al., 2008; Xu and Littman, 1993).

Prior studies suggest that macrocomplexes form constantly, regardless of the peptide content of an MHCII, can signal in response to very weak ligands on thymocytes and that both the TCR-pMHCII dwell time and the frequency of CD4-Lck interactions influence the signaling outcome (Kao and Allen, 2005; Parrish et al., 2016; Stepanek et al., 2014; Wang et al., 2001b). Here and elsewhere, CD4 minimally impacted agonist TCR-pMHCII interactions if only agonist pMHCII is present, indicating there is a TCR dwell time above which CD4 is more likely to cycle through these macrocomplexes than enhance TCR-pMHCII dwell time (Crawford et al., 1998; Hong et al., 2015; Huppa et al., 2010; O'Donoghue et al., 2013; Stepanek et al., 2014; Wooldridge et al., 2006). However, CD4 did influence TCR dwell time on agonist ligands diluted among null ligands— conditions that were not explored in prior studies— suggesting that CD4 can make a relevant contribution to TCR dwell time on agonist pMHCII. Our data also demonstrate that CD4 increases TCR dwell time on low-affinity pMHCII. These results are consistent with biomembrane force probe (BFP) 2D affinity measurements of the 3.L2 TCR that showed no contribution of CD4 to the agonist Hb:I-E^k pMHCII, but a significant contribution to binding of an antagonist (I72) pMHCII and a trend toward significance with a weak agonist ligand (T72; $p = 0.06$) (Hong et al., 2015). Importantly, we found the CD4 dwell time on pMHCII to be proportional to that of the TCR in a bulk assay, yet the CD4 $t_{1/2}$ was always faster than the TCR; therefore, the kinetics of TCR-pMHCII interactions would influence the duration that a docking interface remains intact for CD4 molecules to cycle through in a processive-like manner (Stepanek et al., 2014). By increasing TCR-CD3 dwell time on lower-affinity pMHCII, CD4 might help recruit a greater breadth of clonotypes from the $CD4^+$ T cell repertoire that differentiate to distinct effector phenotypes (Gottschalk et al., 2010; Tubo et al., 2013). This also appears likely to be key for signaling in response to the weak TCR-pMHCII interactions that drive $CD4^+$ T cell development and homeostasis (Kao and Allen, 2005; Parrish et al., 2016; Stepanek et al., 2014; Wang et al., 2001b).

A final implication of this macrocomplex design is that it provides an explanation for how distinct constituents of the TCR repertoire can reproducibly direct the appropriate response to an immunological challenge. At issue is that if TCRs bind pMHCII in a noncanonical orientation, then the docking interface for CD4 would not be formed and any recruitment of Lck to the ITAMs by CD4 would be subject to the problems outlined above for a V-like arch with extraordinarily weak CD4-MHCII interactions. So, if two TCRs interact with the same pMHCII via the same kinetic properties but different docking modalities, then they would likely produce very different outcomes due to differences in both the spatial relationship between Lck and the ITAMs, and the duration with which they are held there. But it is now clear that there is a reliable relationship between the kinetics of TCR-pMHCII interactions and $CD4^+$ T cell signaling, gene expression, and effector functions (Allison et al., 2016; Corse et al., 2010; Gottschalk et al., 2010; Govern et al., 2010; Kersh et al., 1998; Stepanek et al., 2014; Tubo et al., 2013; van Panhuys et al., 2014; Vanguri et al., 2013). Since the highly ordered macrocomplex imposes uniform requirements for assembly on a diverse collection of TCRs within the repertoire, the spatial relationship between Lck and each of the ten ITAMs will always be the same for any TCR that docks appropriately, as supported by our recent FRET analysis (Glassman et al., 2016). Consequently, the quantity and quality of ITAM phosphorylation by CD4-associated Lck would be determined strictly by the kinetic factors that influence the stability of the macrocomplex, and thus the duration of Lck proximity to any given ITAM, as suggested previously (Kersh et al., 1998). We thus postulate that the precise assembly of this molecular machine has evolved as an equalizer that ensures a reproducible translation of information, regarding specificity at the TCR-pMHCII interface, into scalable signaling at the ITAMs; in turn, the extent of ITAM phosphorylation would determine $CD4^+$ T cell responses (Guy et al., 2013; Holst et al., 2008; Hwang et al., 2015). Future experiments will be required to interrogate how these molecular mechanisms influence cell-fate decisions *in vivo*.

EXPERIMENTAL PROCEDURES

Cell lines, constructs, standard experimental procedures, and previously described image acquisition and analysis can be found in Supplemental Experimental Procedures.

Mice

6- to 8-week-old male and female 5c.c7 TCR Tg mice were used for spleenocyte and thymocyte co-cultures. Mice were maintained under specific pathogen-free conditions in the University of Arizona animal facility. Experiments were conducted under the guidelines and approval of the University of Arizona Institutional Animal Care and Use Committee.

Image Analysis

For subunit accumulation, cells were bisected with a line scan ROI in bright field, and the median mEGFP intensity was exported using SlideBook6 (3I). Data were imported into Prism (GraphPad) and displayed as fluorescence intensity.

FRAP analysis was performed as described (Klammt et al., 2015). Background subtracted median fluorescence intensity in the photobleached regions and a 6.45-μm^2 photobleach control region were exported for analysis in MATLAB (MathWorks). Photoablation was calculated as the ratio of postbleach to prebleach fluorescence intensity, $AbI = I^{t=0}/I^{t=-1}$ where $t = -1$ is the time point prior to bleaching and $t = 0$ is first frame postbleach. Analyzed events had photobleaching to <20% of prebleach intensity. Recovery (%) was computed for each time point ($t = x$) as $Recovery = (I^{t=x} - I^{t=0})/(I^{t=-1} - I^{t=0})*100$ where $t = -1$ is the time point prior to bleaching and $t = 0$ is first frame postbleach. FRAP data were fitted with a single-term exponential function, $F = A(1-e^{-kt})$ where F is fluorescence intensity, A is the mobile fraction, t is the elapsed time following photobleaching and k is related to the half-life such that $t_{1/2} = \ln(2)/k$.

Statistical Analysis

Statistical analyses were performed using Prism 6 (GraphPad software) and are indicated in the figure legends along with sample size (n). Data were assessed for normality using a D'Agostino and Pearson omnibus normality test. Data that were normally distributed were further analyzed using a one-way analysis of variance (ANOVA) and Dunnet's multiple comparison test or a t test, as indicated in the figure legends. Nonparametric data were analyzed using a Mann-Whitney test. For FRAP analysis, fit and 95% confidence intervals (CIs) were generated using MATLAB nonlinear fitting (Klammt et al., 2015).

SUPPLEMENTAL INFORMATION

Supplemental Information includes Supplemental Experimental Procedures, seven figures, and two movies and can be found with this article online at https://doi.org/10.1016/j.celrep.2017.12.104.

ACKNOWLEDGMENTS

We thank Morgan Huse, John Purdy, Lonnie Lybarger, Sam Campos, and Janko Nikolich-Zugich for critical feedback on the manuscript as well as members of the Frelinger, Schenten, and Wu labs for thoughtful comments. Jessica Seng, Karen Hernandez, Katrina Lichauco, and Joseph Wagner provided technical assistance. The UACC/ARL Cytometry Core Facility and the Cancer Center Support Grant (CCSG-CA 023074) supported our flow cytometry. M.S.K. is a Pew Scholar in the Biomedical Sciences, supported by The Pew Charitable Trusts. This work was also supported by the University of Arizona College of Medicine (M.S.K.), the Bio5 Institute (M.S.K.), and NIH/NIAID R01AI101053 (M.S.K.).

AUTHOR CONTRIBUTIONS

M.S.K. directed the research. C.R.G., H.L.P., and M.S.K. designed the experiments. C.R.G., H.L.P., and M.S.L. generated key reagents, analytical tools, and conducted the experiments. All authors analyzed the data, wrote the manuscript, and edited the manuscript.

DECLARATION OF INTERESTS

The authors declare no competing interests.

Received: November 29, 2016
Revised: December 7, 2017
Accepted: December 27, 2017
Published: January 30, 2018

REFERENCES

Allison, K.A., Sajti, E., Collier, J.G., Gosselin, D., Troutman, T.D., Stone, E.L., Hedrick, S.M., and Glass, C.K. (2016). Affinity and dose of TCR engagement yield proportional enhancer and gene activity in CD4+ T cells. eLife *5*, Published online July 4, 2016. https://doi.org/10.7554/eLife.10134.

Bain, J., Plater, L., Elliott, M., Shpiro, N., Hastie, C.J., McLauchlan, H., Klevernic, I., Arthur, J.S., Alessi, D.R., and Cohen, P. (2007). The selectivity of protein kinase inhibitors: A further update. Biochem. J. *408*, 297–315.

Call, M.E., Pyrdol, J., Wiedmann, M., and Wucherpfennig, K.W. (2002). The organizing principle in the formation of the T cell receptor-CD3 complex. Cell *111*, 967–979.

Connolly, J.M., Hansen, T.H., Ingold, A.L., and Potter, T.A. (1990). Recognition by CD8 on cytotoxic T lymphocytes is ablated by several substitutions in the class I alpha 3 domain: CD8 and the T-cell receptor recognize the same class I molecule. Proc. Natl. Acad. Sci. USA *87*, 2137–2141.

Corse, E., Gottschalk, R.A., Krogsgaard, M., and Allison, J.P. (2010). Attenuated T cell responses to a high-potency ligand in vivo. PLoS Biol. *8*, Published online September 14, 2010. https://doi.org/10.1371/journal.pbio.1000481.

Crawford, F., Kozono, H., White, J., Marrack, P., and Kappler, J. (1998). Detection of antigen-specific T cells with multivalent soluble class II MHC covalent peptide complexes. Immunity *8*, 675–682.

DeLano, W.L., Ultsch, M.H., de Vos, A.M., and Wells, J.A. (2000). Convergent solutions to binding at a protein-protein interface. Science *287*, 1279–1283.

Ding, Y.H., Baker, B.M., Garboczi, D.N., Biddison, W.E., and Wiley, D.C. (1999). Four A6-TCR/peptide/HLA-A2 structures that generate very different T cell signals are nearly identical. Immunity *11*, 45–56.

Fazilleau, N., McHeyzer-Williams, L.J., Rosen, H., and McHeyzer-Williams, M.G. (2009). The function of follicular helper T cells is regulated by the strength of T cell antigen receptor binding. Nat. Immunol. *10*, 375–384.

Fernandes, R.A., Shore, D.A., Vuong, M.T., Yu, C., Zhu, X., Pereira-Lopes, S., Brouwer, H., Fennelly, J.A., Jessup, C.M., Evans, E.J., et al. (2012). T cell receptors are structures capable of initiating signaling in the absence of large conformational rearrangements. J. Biol. Chem. *287*, 13324–13335.

Garcia, K.C., Teyton, L., and Wilson, I.A. (1999). Structural basis of T cell recognition. Annu. Rev. Immunol. *17*, 369–397.

Gil, D., Schamel, W.W., Montoya, M., Sánchez-Madrid, F., and Alarcón, B. (2002). Recruitment of Nck by CD3 epsilon reveals a ligand-induced conformational change essential for T cell receptor signaling and synapse formation. Cell *109*, 901–912.

Glaichenhaus, N., Shastri, N., Littman, D.R., and Turner, J.M. (1991). Requirement for association of p56lck with CD4 in antigen-specific signal transduction in T cells. Cell *64*, 511–520.

Glassman, C.R., Parrish, H.L., Deshpande, N.R., and Kuhns, M.S. (2016). The CD4 and CD3δε cytosolic juxtamembrane regions are proximal within a compact TCR-CD3-pMHC-CD4 macrocomplex. J. Immunol. *196*, 4713–4722.

Gottschalk, R.A., Corse, E., and Allison, J.P. (2010). TCR ligand density and affinity determine peripheral induction of Foxp3 in vivo. J. Exp. Med. *207*, 1701–1711.

Govern, C.C., Paczosa, M.K., Chakraborty, A.K., and Huseby, E.S. (2010). Fast on-rates allow short dwell time ligands to activate T cells. Proc. Natl. Acad. Sci. USA *107*, 8724–8729.

Guy, C.S., Vignali, K.M., Temirov, J., Bettini, M.L., Overacre, A.E., Smeltzer, M., Zhang, H., Huppa, J.B., Tsai, Y.H., Lobry, C., et al. (2013). Distinct TCR signaling pathways drive proliferation and cytokine production in T cells. Nat. Immunol. *14*, 262–270.

Holst, J., Wang, H., Eder, K.D., Workman, C.J., Boyd, K.L., Baquet, Z., Singh, H., Forbes, K., Chruscinski, A., Smeyne, R., et al. (2008). Scalable signaling mediated by T cell antigen receptor-CD3 ITAMs ensures effective negative selection and prevents autoimmunity. Nat. Immunol. *9*, 658–666.

Hong, J., Persaud, S.P., Horvath, S., Allen, P.M., Evavold, B.D., and Zhu, C. (2015). Force-regulated in situ TCR-peptide-bound MHC class II kinetics determine functions of CD4+ T cells. J. Immunol. *195*, 3557–3564.

Huppa, J.B., Axmann, M., Mörtelmaier, M.A., Lillemeier, B.F., Newell, E.W., Brameshuber, M., Klein, L.O., Schütz, G.J., and Davis, M.M. (2010). TCR-peptide-MHC interactions in situ show accelerated kinetics and increased affinity. Nature *463*, 963–967.

Hwang, S., Palin, A.C., Li, L., Song, K.D., Lee, J., Herz, J., Tubo, N., Chu, H., Pepper, M., Lesourne, R., et al. (2015). TCR ITAM multiplicity is required for the generation of follicular helper T-cells. Nat. Commun. *6*, 6982.

Irvine, D.J., Purbhoo, M.A., Krogsgaard, M., and Davis, M.M. (2002). Direct observation of ligand recognition by T cells. Nature *419*, 845–849.

Janeway, C.A., Jr. (1988). T-cell development. Accessories or coreceptors? Nature *335*, 208–210.

Jönsson, P., Southcombe, J.H., Santos, A.M., Huo, J., Fernandes, R.A., McColl, J., Lever, M., Evans, E.J., Hudson, A., Chang, V.T., et al. (2016). Remarkably low affinity of CD4/peptide-major histocompatibility complex class II protein interactions. Proc. Natl. Acad. Sci. USA *113*, 5682–5687.

Kao, H., and Allen, P.M. (2005). An antagonist peptide mediates positive selection and CD4 lineage commitment of MHC class II-restricted T cells in the absence of CD4. J. Exp. Med. *201*, 149–158.

Kersh, G.J., Kersh, E.N., Fremont, D.H., and Allen, P.M. (1998). High- and low-potency ligands with similar affinities for the TCR: The importance of kinetics in TCR signaling. Immunity *9*, 817–826.

Killeen, N., and Littman, D.R. (1993). Helper T-cell development in the absence of CD4-p56lck association. Nature *364*, 729–732.

Klammt, C., Novotná, L., Li, D.T., Wolf, M., Blount, A., Zhang, K., Fitchett, J.R., and Lillemeier, B.F. (2015). T cell receptor dwell times control the kinase activity of Zap70. Nat. Immunol. *16*, 961–969.

König, R., Huang, L.Y., and Germain, R.N. (1992). MHC class II interaction with CD4 mediated by a region analogous to the MHC class I binding site for CD8. Nature *356*, 796–798.

Krogsgaard, M., Prado, N., Adams, E.J., He, X.L., Chow, D.C., Wilson, D.B., Garcia, K.C., and Davis, M.M. (2003). Evidence that structural rearrangements and/or flexibility during TCR binding can contribute to T cell activation. Mol. Cell *12*, 1367–1378.

Krogsgaard, M., Li, Q.J., Sumen, C., Huppa, J.B., Huse, M., and Davis, M.M. (2005). Agonist/endogenous peptide-MHC heterodimers drive T cell activation and sensitivity. Nature *434*, 238–243.

Kuhns, M.S., and Badgandi, H.B. (2012). Piecing together the family portrait of TCR-CD3 complexes. Immunol. Rev. *250*, 120–143.

Kuhns, M.S., and Davis, M.M. (2007). Disruption of extracellular interactions impairs T cell receptor-CD3 complex stability and signaling. Immunity *26*, 357–369.

Kuhns, M.S., Girvin, A.T., Klein, L.O., Chen, R., Jensen, K.D., Newell, E.W., Huppa, J.B., Lillemeier, B.F., Huse, M., Chien, Y.H., et al. (2010). Evidence for a functional sidedness to the alphabetaTCR. Proc. Natl. Acad. Sci. USA *107*, 5094–5099.

Lee, M.S., Glassman, C.R., Deshpande, N.R., Badgandi, H.B., Parrish, H.L., Uttamapinant, C., Stawski, P.S., Ting, A.Y., and Kuhns, M.S. (2015). A mechanical switch couples T cell receptor triggering to the cytoplasmic juxtamembrane regions of CD3ζζ. Immunity *43*, 227–239.

Lesk, A.M., and Chothia, C. (1988). Elbow motion in the immunoglobulins involves a molecular ball-and-socket joint. Nature *335*, 188–190.

Li, L., Guo, X., Shi, X., Li, C., Wu, W., Yan, C., Wang, H., Li, H., and Xu, C. (2017). Ionic CD3-Lck interaction regulates the initiation of T-cell receptor signaling. Proc. Natl. Acad. Sci. USA *114*, E5891–E5899.

Madrenas, J., Chau, L.A., Smith, J., Bluestone, J.A., and Germain, R.N. (1997). The efficiency of CD4 recruitment to ligand-engaged TCR controls the agonist/partial agonist properties of peptide-MHC molecule ligands. J. Exp. Med. *185*, 219–229.

Malissen, B., and Bongrand, P. (2015). Early T cell activation: Integrating biochemical, structural, and biophysical cues. Annu. Rev. Immunol. *33*, 539–561.

Mingueneau, M., Sansoni, A., Grégoire, C., Roncagalli, R., Aguado, E., Weiss, A., Malissen, M., and Malissen, B. (2008). The proline-rich sequence of CD3epsilon controls T cell antigen receptor expression on and signaling potency in preselection CD4+CD8+ thymocytes. Nat. Immunol. *9*, 522–532.

Minguet, S., Swamy, M., Alarcón, B., Luescher, I.F., and Schamel, W.W. (2007). Full activation of the T cell receptor requires both clustering and conformational changes at CD3. Immunity *26*, 43–54.

Newell, E.W., Ely, L.K., Kruse, A.C., Reay, P.A., Rodriguez, S.N., Lin, A.E., Kuhns, M.S., Garcia, K.C., and Davis, M.M. (2011). Structural basis of specificity and cross-reactivity in T cell receptors specific for cytochrome c-I-E(k). J. Immunol. *186*, 5823–5832.

O'Donoghue, G.P., Pielak, R.M., Smoligovets, A.A., Lin, J.J., and Groves, J.T. (2013). Direct single molecule measurement of TCR triggering by agonist pMHC in living primary T cells. eLife *2*, e00778.

Parrish, H.L., Glassman, C.R., Keenen, M.M., Deshpande, N.R., Bronnimann, M.P., and Kuhns, M.S. (2015). A transmembrane domain GGxxG motif in CD4 contributes to its Lck-independent function but does not mediate CD4 dimerization. PLoS ONE *10*, e0132333.

Parrish, H.L., Deshpande, N.R., Vasic, J., and Kuhns, M.S. (2016). Functional evidence for TCR-intrinsic specificity for MHCII. Proc. Natl. Acad. Sci. USA *113*, 3000–3005.

Roh, K.H., Lillemeier, B.F., Wang, F., and Davis, M.M. (2015). The coreceptor CD4 is expressed in distinct nanoclusters and does not colocalize with T-cell receptor and active protein tyrosine kinase p56lck. Proc. Natl. Acad. Sci. USA *112*, E1604–E1613.

Rossjohn, J., Gras, S., Miles, J.J., Turner, S.J., Godfrey, D.I., and McCluskey, J. (2015). T cell antigen receptor recognition of antigen-presenting molecules. Annu. Rev. Immunol. *33*, 169–200.

Savage, P.A., Boniface, J.J., and Davis, M.M. (1999). A kinetic basis for T cell receptor repertoire selection during an immune response. Immunity *10*, 485–492.

Spangler, J.B., Moraga, I., Mendoza, J.L., and Garcia, K.C. (2015). Insights into cytokine-receptor interactions from cytokine engineering. Annu. Rev. Immunol. *33*, 139–167.

Stepanek, O., Prabhakar, A.S., Osswald, C., King, C.G., Bulek, A., Naeher, D., Beaufils-Hugot, M., Abanto, M.L., Galati, V., Hausmann, B., et al. (2014). Coreceptor scanning by the T cell receptor provides a mechanism for T cell tolerance. Cell *159*, 333–345.

Sun, Z.J., Kim, K.S., Wagner, G., and Reinherz, E.L. (2001). Mechanisms contributing to T cell receptor signaling and assembly revealed by the solution structure of an ectodomain fragment of the CD3 epsilon gamma heterodimer. Cell *105*, 913–923.

Tubo, N.J., Pagán, A.J., Taylor, J.J., Nelson, R.W., Linehan, J.L., Ertelt, J.M., Huseby, E.S., Way, S.S., and Jenkins, M.K. (2013). Single naive CD4+ T cells from a diverse repertoire produce different effector cell types during infection. Cell *153*, 785–796.

van Panhuys, N., Klauschen, F., and Germain, R.N. (2014). T-cell-receptor-dependent signal intensity dominantly controls CD4(+) T cell polarization In Vivo. Immunity *41*, 63–74.

Vanguri, V., Govern, C.C., Smith, R., and Huseby, E.S. (2013). Viral antigen density and confinement time regulate the reactivity pattern of CD4 T-cell responses to vaccinia virus infection. Proc. Natl. Acad. Sci. USA *110*, 288–293.

Vidal, K., Daniel, C., Hill, M., Littman, D.R., and Allen, P.M. (1999). Differential requirements for CD4 in TCR-ligand interactions. J. Immunol. *163*, 4811–4818.

Vignali, D.A., and Vignali, K.M. (1999). Profound enhancement of T cell activation mediated by the interaction between the TCR and the D3 domain of CD4. J. Immunol. *162*, 1431–1439.

Vignali, D.A., Carson, R.T., Chang, B., Mittler, R.S., and Strominger, J.L. (1996). The two membrane proximal domains of CD4 interact with the T cell receptor. J. Exp. Med. *183*, 2097–2107.

Wang, J.H., Meijers, R., Xiong, Y., Liu, J.H., Sakihama, T., Zhang, R., Joachimiak, A., and Reinherz, E.L. (2001a). Crystal structure of the human CD4 N-terminal two-domain fragment complexed to a class II MHC molecule. Proc. Natl. Acad. Sci. USA *98*, 10799–10804.

Wang, Q., Strong, J., and Killeen, N. (2001b). Homeostatic competition among T cells revealed by conditional inactivation of the mouse Cd4 gene. J. Exp. Med. *194*, 1721–1730.

Wang, X., Lupardus, P., Laporte, S.L., and Garcia, K.C. (2009). Structural biology of shared cytokine receptors. Annu. Rev. Immunol. *27*, 29–60.

Wooldridge, L., Scriba, T.J., Milicic, A., Laugel, B., Gostick, E., Price, D.A., Phillips, R.E., and Sewell, A.K. (2006). Anti-coreceptor antibodies profoundly affect staining with peptide-MHC class I and class II tetramers. Eur. J. Immunol. *36*, 1847–1855.

Wu, L.C., Tuot, D.S., Lyons, D.S., Garcia, K.C., and Davis, M.M. (2002). Two-step binding mechanism for T-cell receptor recognition of peptide MHC. Nature *418*, 552–556.

Xu, H., and Littman, D.R. (1993). A kinase-independent function of Lck in potentiating antigen-specific T cell activation. Cell *74*, 633–643.

Xu, C., Call, M.E., and Wucherpfennig, K.W. (2006). A membrane-proximal tetracysteine motif contributes to assembly of CD3deltaepsilon and CD3gammaepsilon dimers with the T cell receptor. J. Biol. Chem. *281*, 36977–36984.

Yin, Y., Wang, X.X., and Mariuzza, R.A. (2012). Crystal structure of a complete ternary complex of T-cell receptor, peptide-MHC, and CD4. Proc. Natl. Acad. Sci. USA *109*, 5405–5410.

Zhu, J., Yamane, H., and Paul, W.E. (2010). Differentiation of effector CD4 T cell populations (*). Annu. Rev. Immunol. *28*, 445–489.

Zuñiga-Pflücker, J.C., McCarthy, S.A., Weston, M., Longo, D.L., Singer, A., and Kruisbeek, A.M. (1989). Role of CD4 in thymocyte selection and maturation. J. Exp. Med. *169*, 2085–2096.

Cell Reports, Volume *22*

Supplemental Information

Reciprocal TCR-CD3 and CD4 Engagement of a Nucleating pMHCII Stabilizes a Functional Receptor Macrocomplex

Caleb R. Glassman, Heather L. Parrish, Mark S. Lee, and Michael S. Kuhns

SUPPLEMENTAL EXPERIMENTAL PROCEDURES

Cell lines and constructs

58$\alpha^-\beta^-$ and M12 cells were generated by retroviral transduction using the MSCV-based retroviral expression vectors pP2 (IRES-puromycin resistance) and pZ4 (IRES-zeocin resistance) (Glassman et al., 2016; Lee et al., 2015; Parrish et al., 2016).

Proteins encoded by the constructs used in this study are described by amino acid (aa) number beginning at the start methionine (UniProt convention). Constructs encoding cDNA for the B3K506 and B3K508 TCRs were kindly provided by Eric Huseby and used for PCR amplification for cloning into pP2 (TCRβ) and pZ4 (TCRα). The 5c.c7 or 2B4 TCR, which are specific for moth cytochrome c (88-103) presented in I-E^k, or the B3K506 or B3K508 TCRs specific for the 3K peptide presented in I-A^b were expressed with full length or C-terminally truncated CD3 subunits (CD3δT aa:1-132, CD3γT aa:1-143, CD3εT aa:1-139, and CD3ζT aa:1-57) along with a C-terminally truncated CD4 (CD4T aa:1-421)(Glassman et al., 2016). CD4T variants used in this study were $CD4T^{\Delta bind}$ (aa: 68-73 KGVLIR to DGDSDS), $CD4T^{P228E+F231E}$ and $CD4T^{P281E}$.

For 58$\alpha^-\beta^-$ lines, the C-terminus of the 5c.c7 α chain, 2B4 β chain, B3K506 β chain or B3K508 β chain was fused to mEGFP via a long flexible linker (AAAGGGGSGGGGSGGGGS), the 5c.c7 β chain, 2B4 α chain, B3K506 α chain, B3K508 α chain and CD4T were encoded by independent constructs and full-length CD3 subunits were encoded by a poly-cistronic construct as previously described (Glassman et al., 2016; Parrish et al., 2016).

5c.c7$^+$ M12 lines were generated using constructs encoding CD3εT-T2A-5c.c7α, CD3ζT-T2A-5c.c7β, $CD3\delta T^G$-T2A-CD3γT and $CD4T^{mCh}$. CD3δT was fused to mEGFP via a flexible GGSAAG linker and CD4 was fused to mCherry via an AAAG linker as previously described (Glassman et al., 2016). CD3ζT was fused via a GGSAAG linker to the biotin acceptor peptide, AP-3, a short tag that was considered irrelevant for the current study. 2B4$^+$ M12 lines were generated using constructs encoding 2B4α, $2B4\beta^G$, $CD4T^{mCh}$, and a polycystronic construct encoding C-terminally truncated CD3 subunits. The 2B4 β chain was fused to mEGFP via a long flexible linker (AAAGGGGSGGGGSGGGGS) and CD4 was fused to mCherry via an AAAG linker as previously described (Glassman et al., 2016).

APCs were generated by transducing M12 or 58$\alpha^-\beta^-$ cells with full-length I-$E^k\alpha$ or I-$A^b\alpha$ and full-length I-$E^k\beta$ or I-$A^b\beta$ fused via the N-terminus to a peptide as previously described (Parrish et al., 2016; Parrish et al., 2015). Peptides bound to I-E^k in this study were moth cytochrome c (MCC 88-103), the altered peptide ligands T102S and

T102G, and the mouse hemoglobin d allele (Hb 64-76). Peptides bound to I-A^b in this study were Ova 326-338, 3K and the altered peptide ligands P-1A and P5R (Huseby et al., 2006).

Cell surface expression of CD4 (mAb clone GK1.5 e450 eBioscience), TCRα (Vα11, mAb clone RR8-1 allophycocyanin eBioscience), TCRβ (Vβ3, mAb clone KJ25 PE BD Biosciences), I-E^k (mAb clone 14-4-4S) and I-A^b (mAb clone KH74) were determined by flow cytometry as indicated in the figures. The P281E mutation reduced cell surface expression on 58$\alpha^-\beta^-$ cells, so lines were FACS sorted using a non-blocking CD4 antibody (mAb clone RM4-4 PE Biolegend).

Functional assays

For peptide titration experiments, 5 X 10^4 5c.c7 TCR transgenic spleenocytes or thymocytes or 5 X 10^4 58$\alpha^-\beta^-$ cells were co-cultured with 1 X 10^5 M12 I-E^k cells and MCC 88-103, T102S, or T102G peptide at the indicated concentration in 96-well round-bottom plates and peptides were purchased at ninety percent purity from 21st Century Biochemicals, Inc. In indicated experiments, anti-CD4 (mAb clone GK1.5) or anti-CD8 (control, mAb clone 53.6-7) was added at 20μg/mL. Supernatants were harvested for IL-2 ELISA after 16 hours co-culture as described below. Thymocyte co-cultures were incubated for 14 hours at 37°C and stained for Vα11 (mAb clone RR8-1, APC, eBiosciences), CD8β (mAb clone YTS156.7.7, PerCpCy5.5, Biolegend), CD4 (mAb clone Rm4-4, Pacific Blue, Biolegend), CD69 (mAb clone H1-2F3, PE, eBiosciences) and AnnexinV (FITC, Biolegend). For tethered peptide co-cultures, 5 X 10^4 58$\alpha^-\beta^-$ cells were cultured with 1 X 10^5 M12 cells expressing I-E^k tethered to MCC, T102S, T102G or Hb in 96-well round-bottom plates. IL-2 was normalized to the CD4T control for each set of cell lines within each condition to allow for comparison between multiple independently generated cell lines. IL-2 was quantified by ELISA from supernatants after 16 hours co-culture at 37°C for all experiments. Anti-mouse IL-2 (clone JES6-1A12, Biolegend) was used as a capture antibody and biotin anti-mouse IL-2 (clone JES6-5H4, Biolegend) was used as the secondary antibody. Streptavidin-HRP and TMB substrate (Biolegend) were used for detection.

TCR downregulation and CD69 upregulation were measured on T cell hybridomas following 16 hours of co-culture with M12 cells. Cells were pipetted to break apart M12:58$\alpha^-\beta^-$ cell couples, incubated in mAb clone 2.4G2 supernatant to block Fc receptors, and then stained with anti-CD4 (clone GK1.5, e450), CD69 (clone H1.2F3, PE) and Vα11 (clone RR8-1, APC) mAbs. CD69 or Vα11 gMFI was determined for GFP positive and CD4

expression matched 58$\alpha^-\beta^-$ cells and normalized to the gMFI of cells cultured with the Hb:I-E^k controls for each cell line.

Cell coupling

TCR^+ cells expressing mEGFP were combined with Tag-It Violet (Biolegend) loaded APCs expressing tethered pMHCII at a 1:1 ratio. Cells were incubated for 1 hour at 37°C and analyzed by flow cytometry (Egen and Allison, 2002). Couple formation was assessed as the ratio of GFP (TCR^+) Violet ($pMHCII^+$) double positive events divided by the total number of GFP positive events. This was then normalized to CD4T cells interacting with MCC:I-E^k or 3K:I-A^b expressing APCs to allow comparison between multiple experiments. In some experiments, kinase activity was blocked by incubating cells with 20μM PP2 (Calbiochem) or DMSO vehicle control (0.2%) for 20 minutes at 37°C prior to cell coupling.

Soluble proteins for bilayers and immobile surfaces

ICAM-1 and pMHCII production were described previously (Glassman et al., 2016).

Lipid bilayers

Unilaminar vesicles were generated by extruding a lipid mixture consisting of 97.5mol % POPC, 1 mol % DGS NiNTA, 1 mol biotin-CAP PE and 0.5 mol % DOPE-PEG5000 (Avanti Polar Lipids) (Glassman et al., 2016). Bilayers were formed on cleaned glass coverslips and functionalized with 0.05 μg/well MCC:I-E^k and 0.08μg/well ICAM-1 to give a pMHCII density of ~60molecules/μm^2.

Immobile surfaces

Biotinylated poly-L-lysine coated coverslips were coated with 5μg/mL streptavidin, washed and incubated with 5μg/mL pMHCII biotin plus 0.5μg/mL biotinylated anti H2-D^d, which was used to ensure cell attachment (Glassman et al., 2016; Huse et al., 2007).

Microscopy

Total internal reflection fluorescence microscopy (TIRFM) was performed as previously described (Glassman et al., 2016). In brief, cells were allowed to interact with the imaging surface for 20' prior and then imaged for 20-30'.

Data were collected with a Marianas workstation built on a Zeiss Axio Observer Z1 (Intelligent Imaging Innovations, 3I) using a 63x Zeiss TIRF objective coupled to a Zeiss motorized TIRF slider (numerical aperture 1.46). Illumination was achieved with a Laser Stack (3I) containing 50mW 488nm and 561 solid-state lasers at 20% output. Photoablation was performed using a Vector high-speed point scanner (3I) at 100% laser power within a 6.45μm^2 region of interest (ROI) and images were collected using a Photometrics Evolve EMCCD camera (1 pixel= 0.25μm (H) x 0.25μm (V)). Receptor accumulation images consisted of TIRF and brightfield images collected at a single time point. For Fluorescence Recovery After Photobleaching (FRAP) acquisitions, fluorescence images were acquired at 3 sec intervals. Donor Recovery after Acceptor Photobleaching images were acquired at 500ms intervals.

$FRET_E$ analysis

Donor Recovery after Acceptor Photobleaching was performed as previously described (Glassman et al., 2016). Analyzed cells had bleaching below 12.5% of prebleach mCherry intensity. Subsets were matched for mCherry intensity, mEGFP intensity (postbleach) and mEGFP/mCherry ratio in TIRF. FRET efficiency ($FRET_E$) was calculated using: $FRET_E = 1 - Q/DQ$ where Q is the mEGFP intensity prior to photobleaching and DQ is the mEGFP intensity following mCherry ablation.

SUPPLEMTAL REFERENCES

Aivazian, D., and Stern, L.J. (2000). Phosphorylation of T cell receptor zeta is regulated by a lipid dependent folding transition. Nat Struct Biol *7*, 1023-1026.

Egen, J.G., and Allison, J.P. (2002). Cytotoxic T lymphocyte antigen-4 accumulation in the immunological synapse is regulated by TCR signal strength. Immunity *16*, 23-35.

Glassman, C.R., Parrish, H.L., Deshpande, N.R., and Kuhns, M.S. (2016). The CD4 and CD3deltaepsilon Cytosolic Juxtamembrane Regions Are Proximal within a Compact TCR-CD3-pMHC-CD4 Macrocomplex. J Immunol *196*, 4713-4722.

Huppa, J.B., Axmann, M., Mortelmaier, M.A., Lillemeier, B.F., Newell, E.W., Brameshuber, M., Klein, L.O., Schutz, G.J., and Davis, M.M. (2010). TCR-peptide-MHC interactions in situ show accelerated kinetics and increased affinity. Nature *463*, 963-967.

Huse, M., Klein, L.O., Girvin, A.T., Faraj, J.M., Li, Q.J., Kuhns, M.S., and Davis, M.M. (2007). Spatial and temporal dynamics of T cell receptor signaling with a photoactivatable agonist. Immunity *27*, 76-88.

Huseby, E.S., Crawford, F., White, J., Marrack, P., and Kappler, J.W. (2006). Interface-disrupting amino acids establish specificity between T cell receptors and complexes of major histocompatibility complex and peptide. Nat Immunol *7*, 1191-1199.

Jonsson, P., Southcombe, J.H., Santos, A.M., Huo, J., Fernandes, R.A., McColl, J., Lever, M., Evans, E.J., Hudson, A., Chang, V.T.*, et al.* (2016). Remarkably low affinity of CD4/peptide-major histocompatibility complex class II protein interactions. Proc Natl Acad Sci U S A *113*, 5682-5687.

Kuhns, M.S., and Badgandi, H.B. (2012). Piecing together the family portrait of TCR-CD3 complexes. Immunol Rev *250*, 120-143.

Lee, M.S., Glassman, C.R., Deshpande, N.R., Badgandi, H.B., Parrish, H.L., Uttamapinant, C., Stawski, P.S., Ting, A.Y., and Kuhns, M.S. (2015). A Mechanical Switch Couples T Cell Receptor Triggering to the Cytoplasmic Juxtamembrane Regions of CD3zetazeta. Immunity *43*, 227-239.

Nika, K., Soldani, C., Salek, M., Paster, W., Gray, A., Etzensperger, R., Fugger, L., Polzella, P., Cerundolo, V., Dushek, O.*, et al.* (2010). Constitutively active Lck kinase in T cells drives antigen receptor signal transduction. Immunity *32*, 766-777.

Parrish, H.L., Deshpande, N.R., Vasic, J., and Kuhns, M.S. (2016). Functional evidence for TCR-intrinsic specificity for MHCII. Proc Natl Acad Sci U S A.

Parrish, H.L., Glassman, C.R., Keenen, M.M., Deshpande, N.R., Bronnimann, M.P., and Kuhns, M.S. (2015). A Transmembrane Domain GGxxG Motif in CD4 Contributes to Its Lck-Independent Function but Does Not Mediate CD4 Dimerization. PLoS One *10*, e0132333.

Shi, X., Bi, Y., Yang, W., Guo, X., Jiang, Y., Wan, C., Li, L., Bai, Y., Guo, J., Wang, Y.*, et al.* (2013). Ca2+ regulates T-cell receptor activation by modulating the charge property of lipids. Nature *493*, 111-115.

Vignali, D.A., and Vignali, K.M. (1999). Profound enhancement of T cell activation mediated by the interaction between the TCR and the D3 domain of CD4. J Immunol *162*, 1431-1439.

Wang, J.H., Meijers, R., Xiong, Y., Liu, J.H., Sakihama, T., Zhang, R., Joachimiak, A., and Reinherz, E.L. (2001). Crystal structure of the human CD4 N-terminal two-domain fragment complexed to a class II MHC molecule. Proc Natl Acad Sci U S A *98*, 10799-10804.

Xu, C., Gagnon, E., Call, M.E., Schnell, J.R., Schwieters, C.D., Carman, C.V., Chou, J.J., and Wucherpfennig, K.W. (2008). Regulation of T cell receptor activation by dynamic membrane binding of the CD3epsilon cytoplasmic tyrosine-based motif. Cell *135*, 702-713.

Yin, Y., Wang, X.X., and Mariuzza, R.A. (2012). Crystal structure of a complete ternary complex of T-cell receptor, peptide-MHC, and CD4. Proceedings of the National Academy of Sciences of the United States of America *109*, 5405-5410.

Zhang, H., Cordoba, S.P., Dushek, O., and Anton van der Merwe, P. (2011). Basic residues in the T-cell receptor zeta cytoplasmic domain mediate membrane association and modulate signaling. Proceedings of the National Academy of Sciences of the United States of America *108*, 19323-19328.

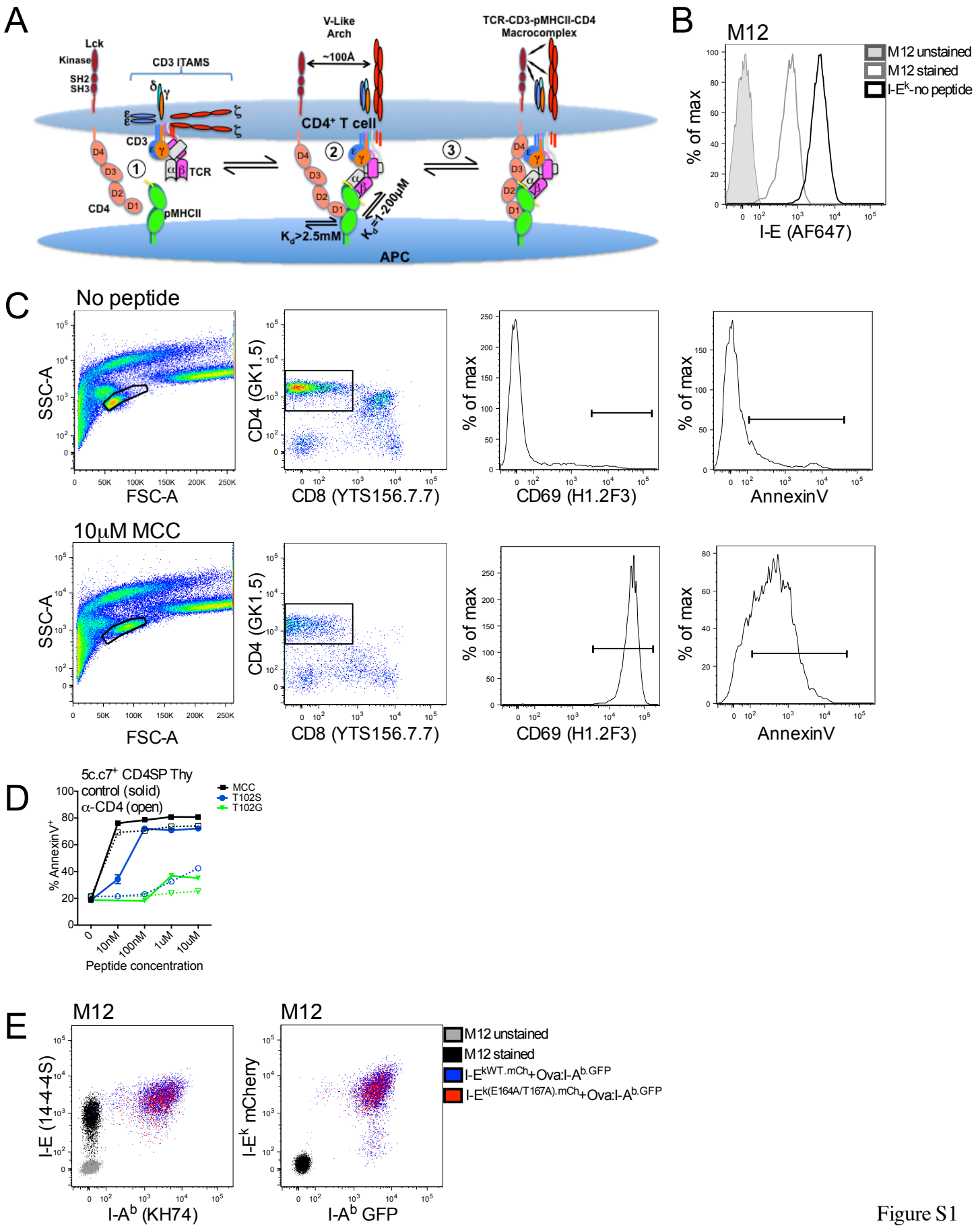
A
Lck
Kinase
SH2
SH3
CD3 ITAMS
V-Like
Arch
~100Å
TCR-CD3-pMHCII-CD4
Macrocomplex
CD4+ T cell
CD3
TCR
CD4
pMHCII
APC
K_d>2.5mM
K_d=1-200μM
B
M12
M12 unstained
M12 stained
I-E^k-no peptide
% of max
I-E (AF647)
C
No peptide
10μM MCC
SSC-A
FSC-A
CD4 (GK1.5)
CD8 (YTS156.7.7)
% of max
CD69 (H1.2F3)
AnnexinV
D
5c.c7$^+$ CD4SP Thy
control (solid)
α-CD4 (open)
MCC
T102S
T102G
% AnnexinV$^+$
Peptide concentration
0
10nM
100nM
1uM
10uM
E
M12
M12
I-E (14-4-4S)
I-A^b (KH74)
I-E^k mCherry
I-A^b GFP
M12 unstained
M12 stained
I-E$^{kWT.mCh}$+Ova:I-A$^{b.GFP}$
I-E$^{k(E164A/T167A).mCh}$+Ova:I-A$^{b.GFP}$

Figure S1

Figure S1. Models and cellular characterization, related to Figure 1.
(**A**) Graphical model depicting the possible assembly of a TCR-CD3-pMHCII-CD4 macrocomplex. (**1**) The unengaged TCR-CD3 complex is shown with CD3ε and CD3ζζ ITAMs associated with the inner leaf of the T cell membrane (Aivazian and Stern, 2000; Shi et al., 2013; Xu et al., 2008). CD4 is shown associated with an active Lck on a T cell surface (upper blue sphere)(Nika et al., 2010). The surface of an APC (lower blue sphere) is shown with a pMHCII. (**2**) The V-like arch model is shown as possible intermediate in the formation of a compact macrocomplex (Wang et al., 2001; Yin et al., 2012). The solution K_d are noted for CD4-MHCII and agonist to weak agonist TCR-pMHCII interactions (Huppa et al., 2010; Jonsson et al., 2016). the ITAMs are shown free of the membrane based on previous studies (Shi et al., 2013; Xu et al., 2008; Zhang et al., 2011). (**3**) The final subunit assembly of a compact TCR-CD3-pMHCII-CD4 macrocomplex (Kuhns and Badgandi, 2012). The low affinity of CD4-MHCII interactions in the D1 domain would allow CD4 to dock along the composite surface of the TCR-CD3-pMHCII axis created by TCR-pMHCII interactions. This is proposed to position Lck in the proper spatial relationship with the ITAMs for the appropriate duration to initiate signaling.
(**B**) Surface expression of I-E^k on M12 I-E^{k+} cells.
(**C**) Gating scheme for CD69 and AnnexinV levels on $CD4^+$ 5c.c7 TCR tg thymocytes. Total thymocytes were cultured with I-E^{k+} M12 cells and a titration of the indicated peptides for 14 hours prior to analysis.
(**D**) Percent of $CD4^+$ 5c.c7 TCR tg thymocytes that were $AnnexinV^+$. Data from C and D are representative of three experiments.
(**E**) Expression of I-E^k and I-A^b on M12 cells expressing I-$E^{k.WT.mCh}$ or I-$E^{k.E164A/T167A.mCh}$ and I-$A^{b.GFP}$-Ova.

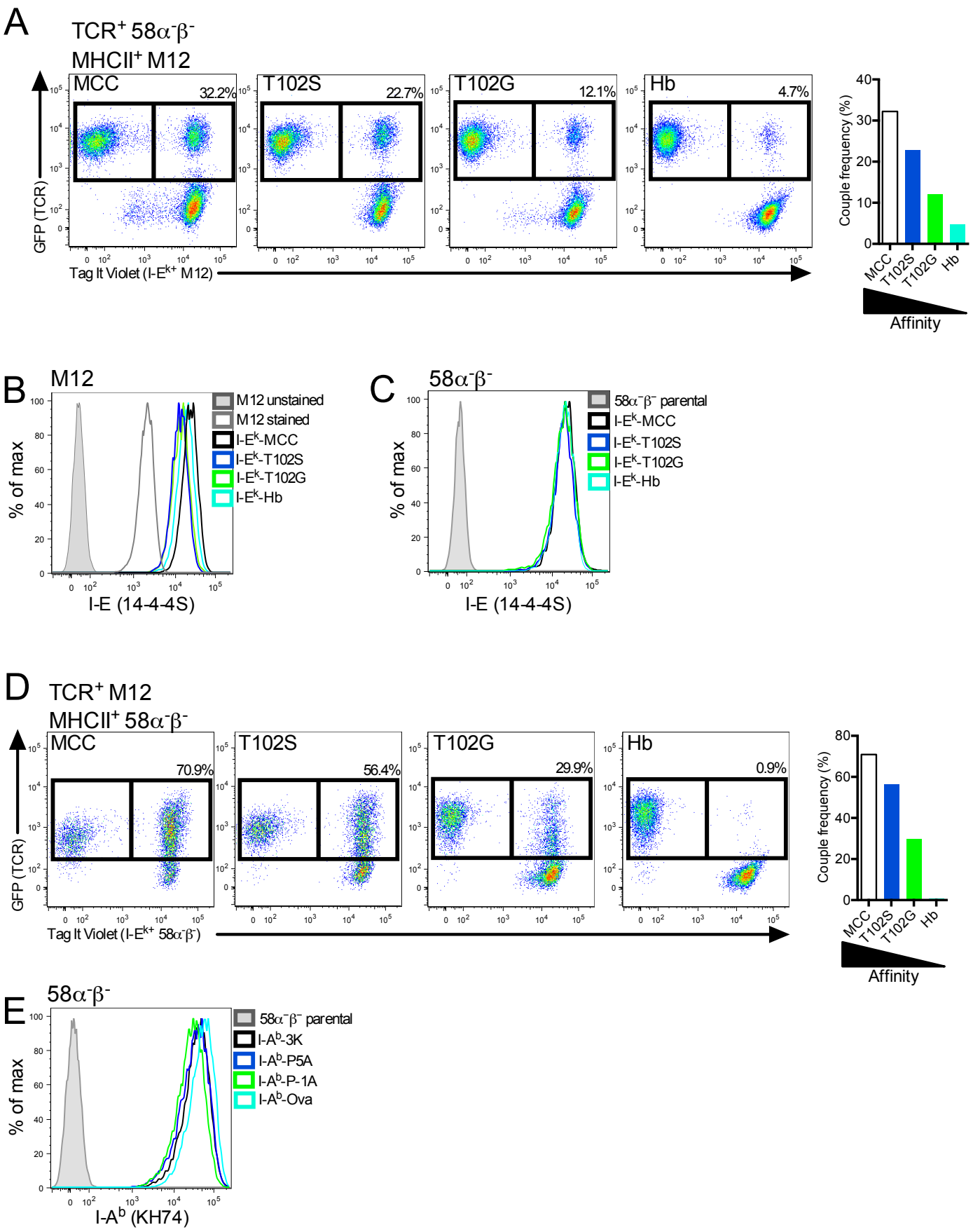
A
TCR+ 58α-β-
MHCII+ M12
MCC
32.2%
T102S
22.7%
T102G
12.1%
Hb
4.7%
GFP (TCR)
Tag It Violet (I-Ek+ M12)
Couple frequency (%)
MCC
T102S
T102G
Hb
Affinity
B
M12
% of max
M12 unstained
M12 stained
I-Ek-MCC
I-Ek-T102S
I-Ek-T102G
I-Ek-Hb
I-E (14-4-4S)
C
58α-β-
58α-β- parental
I-Ek-MCC
I-Ek-T102S
I-Ek-T102G
I-Ek-Hb
I-E (14-4-4S)
D
TCR+ M12
MHCII+ 58α-β-
MCC
70.9%
T102S
56.4%
T102G
29.9%
Hb
0.9%
GFP (TCR)
Tag It Violet (I-Ek+ 58α-β-)
Couple frequency (%)
MCC
T102S
T102G
Hb
Affinity
E
58α-β-
% of max
58α-β- parental
I-Ab-3K
I-Ab-P5A
I-Ab-P-1A
I-Ab-Ova
I-Ab (KH74)

Figure S2

Figure S2. Cell-cell coupling, related to Figure 2.

(**A**) Representative dot plots and quantification of 5c.c7^{+} 58$\alpha^{-}\beta^{-}$ cells expressing TCRα^{G} incubated with M12 cells expressing the indicated tethered pMHCII. Data are representative of three experiments.

(**B-C**) Expression of tethered-pMHCII on I-E^{k+} (**B**) M12 or (**C**) 58$\alpha^{-}\beta^{-}$ cells.

(**D**) Representative dot plots and quantification of 5c.c7^{+} M12 cells expressing CD3T subunits with CD3δT^{G} and CD4T incubated with 58$\alpha^{-}\beta^{-}$ cells expressing I-E^{k} and the indicated tethered peptide. Data are representative of three experiments.

(**E**) Expression of tethered-pMHCII on I-A^{b+} 58$\alpha^{-}\beta^{-}$ cells.

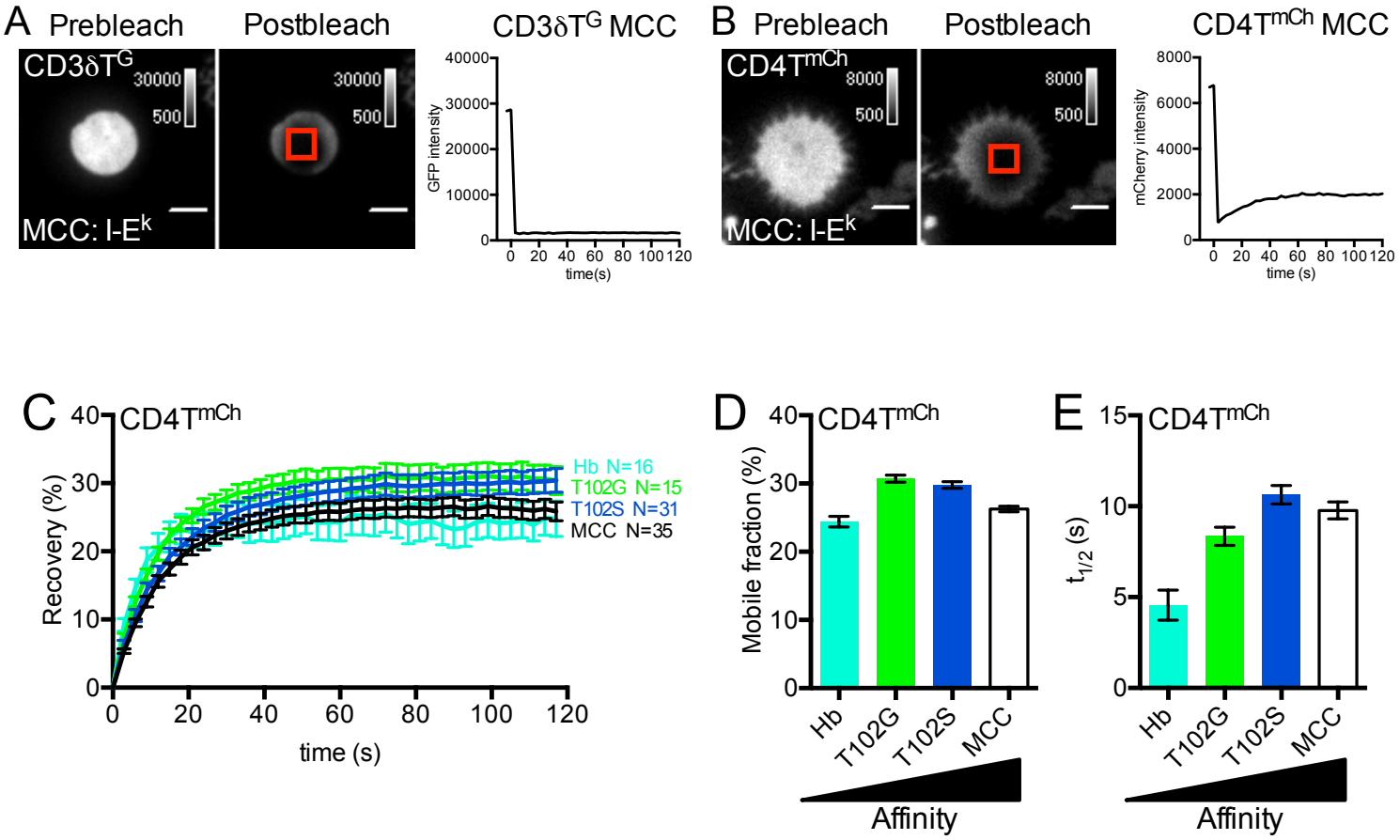
A
Prebleach
Postbleach
CD3δT^G MCC
CD3δT^G
30000
500
MCC: I-E^k
GFP intensity
time(s)
B
Prebleach
Postbleach
CD4T^mCh MCC
CD4T^mCh
8000
500
MCC: I-E^k
mCherry intensity
time (s)
C
CD4T^mCh
Recovery (%)
time (s)
Hb N=16
T102G N=15
T102S N=31
MCC N=35
D
CD4T^mCh
Mobile fraction (%)
Hb
T102G
T102S
MCC
Affinity
E
CD4T^mCh
t1/2 (s)
Hb
T102G
T102S
MCC
Affinity

Figure S3

Figure S3. Fluorescence recovery after photobleaching, related to Figure 3.
(**A-B**) Representative images and quantification of FRAP. 5c.c7^{+} M12 cells expressing CD3T subunits with CD3δT^{G} and CD4T^{mCh} were adhered to immobile surfaces presenting MCC:I-E^{k} for 20' prior to acquisition. Background subtracted TIRF images of (**A**) CD3δT^{G} and (**B**) CD4T^{mCh} before and after photobleaching with 488 and 561nm laser light, respectively. Traces show quantification of red-boxed region of interest (ROI) for 2 min at 3 second intervals following photobleaching. Scale bars represent 5μm and look up tables indicate fluorescence intensity of the photobleached channel.
(**C-H**) FRAP analysis of 2B4^{+} M12 cells expressing truncated CD3 subunits and CD4T^{mCh}. Cells were adhered to I-E^{k} coated surfaces presenting the indicated peptide. (**C**) Recovery traces for mCherry represent mean ± SEM for the indicated number of cells. (**D**) Mobile fraction (%) and (**E**) half-life ($t_{1/2}$) for recovery were determined by curve fitting. Error bars indicate 95% confidence interval.

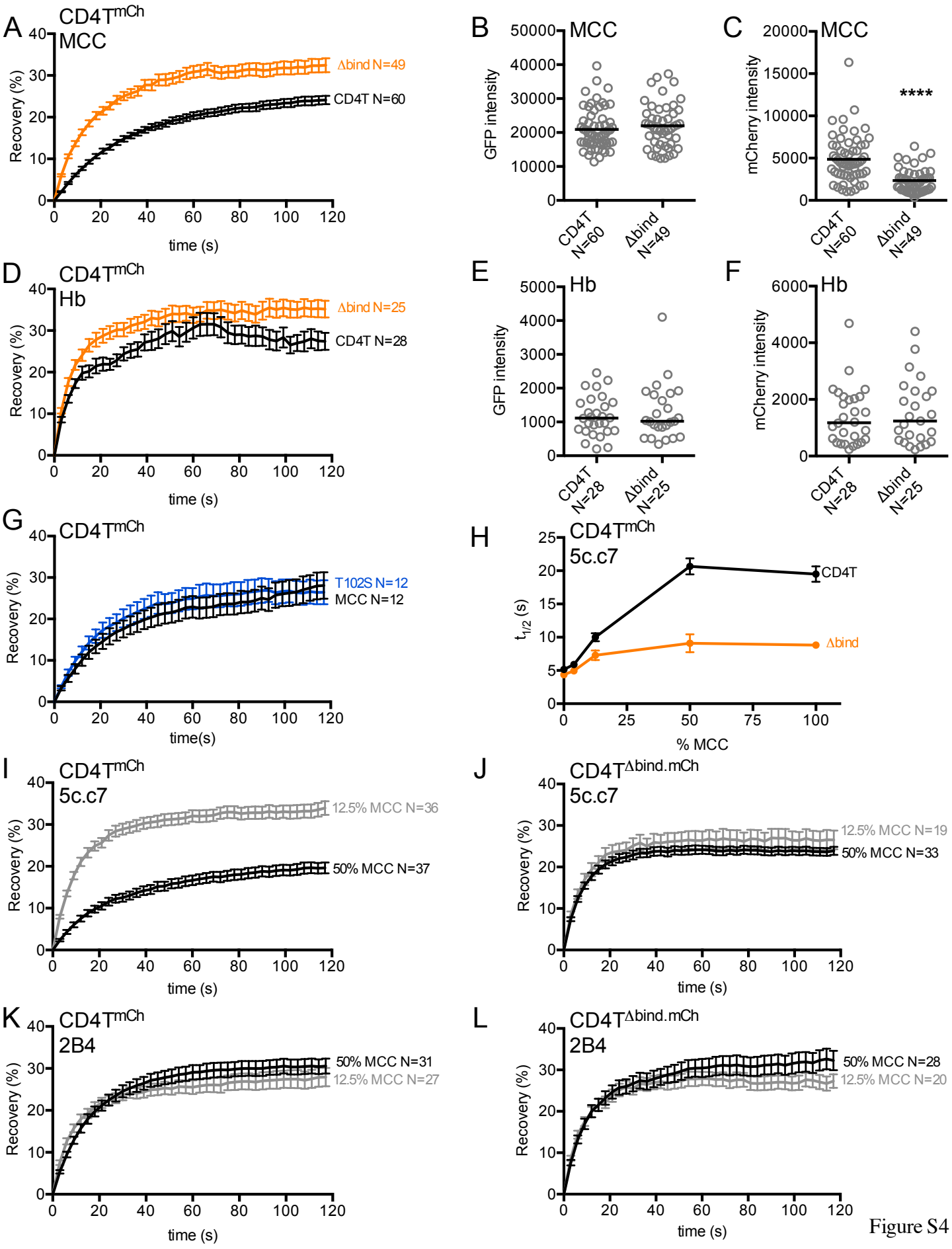
A
CD4T^mCh
MCC
Recovery (%)
time (s)
Δbind N=49
CD4T N=60
B
MCC
GFP intensity
CD4T N=60
Δbind N=49
C
MCC
mCherry intensity
****
CD4T N=60
Δbind N=49
D
CD4T^mCh
Hb
Recovery (%)
time (s)
Δbind N=25
CD4T N=28
E
Hb
GFP intensity
CD4T N=28
Δbind N=25
F
Hb
mCherry intensity
CD4T N=28
Δbind N=25
G
CD4T^mCh
Recovery (%)
time(s)
T102S N=12
MCC N=12
H
CD4T^mCh
5c.c7
t1/2 (s)
% MCC
CD4T
Δbind
I
CD4T^mCh
5c.c7
Recovery (%)
time (s)
12.5% MCC N=36
50% MCC N=37
J
CD4T^Δbind.mCh
5c.c7
Recovery (%)
time (s)
12.5% MCC N=19
50% MCC N=33
K
CD4T^mCh
2B4
Recovery (%)
time (s)
50% MCC N=31
12.5% MCC N=27
L
CD4T^Δbind.mCh
2B4
Recovery (%)
time (s)
50% MCC N=28
12.5% MCC N=20

Figure S4

Figure S4. CD4 recovery, related to Figure 4.
(A-F) CD4 recovery of 5c.c7^{+} M12 cells expressing truncated CD3 subunits with CD3δT^{G} and CD4T^{mCh} or CD4T$^{\Delta bind.\ mCh}$. Cells were adhered to immobile surfaces coated with MCC:I-E^{k} (**A-C**) or Hb:I-E^{k} (**D-F**). Panels on the left show recovery of CD4T^{mCh}. Right-hand panels show mCh intensity prebleach and GFP intensity postbleach. Data correspond to bar graphs in Figure 4A-D.
(**G**) CD4T recovery of pairwise matched 5c.c7^{+} M12 cells as shown in Figure 4E-H.
(**H-L**) CD4T recovery in response to varying doses of MCC:I-E^{k}. 5c.c7^{+} (**H,I,J**) or 2B4^{+} (**K,L**) M12 cells were adhered to immobile surfaces coated with the indicated proportion of MCC:I-E^{k} diluted into Hb:I-E^{k}. **(I-L)** Data correspond to bar graphs in Figure 4I-L. For all data but H, N = number of cells analyzed. For (**H**), dots equal mean +/- SEM for the $t_{1/2}$ values determined in multiple individual experiments. For CD4T^{mCh+}: N=16 (100%); N=4 (50%); N=3 (12.5%); N=1 (4%); N=6 (0%) individual experiments. For CD4T$^{\Delta bind.\ mCh+}$: N=17 (100%); N=4 (50%); N=3 (12.5%); N=1 (4%); N=6 (0%) individual experiments. Between 20-60 cells were analyzed per experiment.

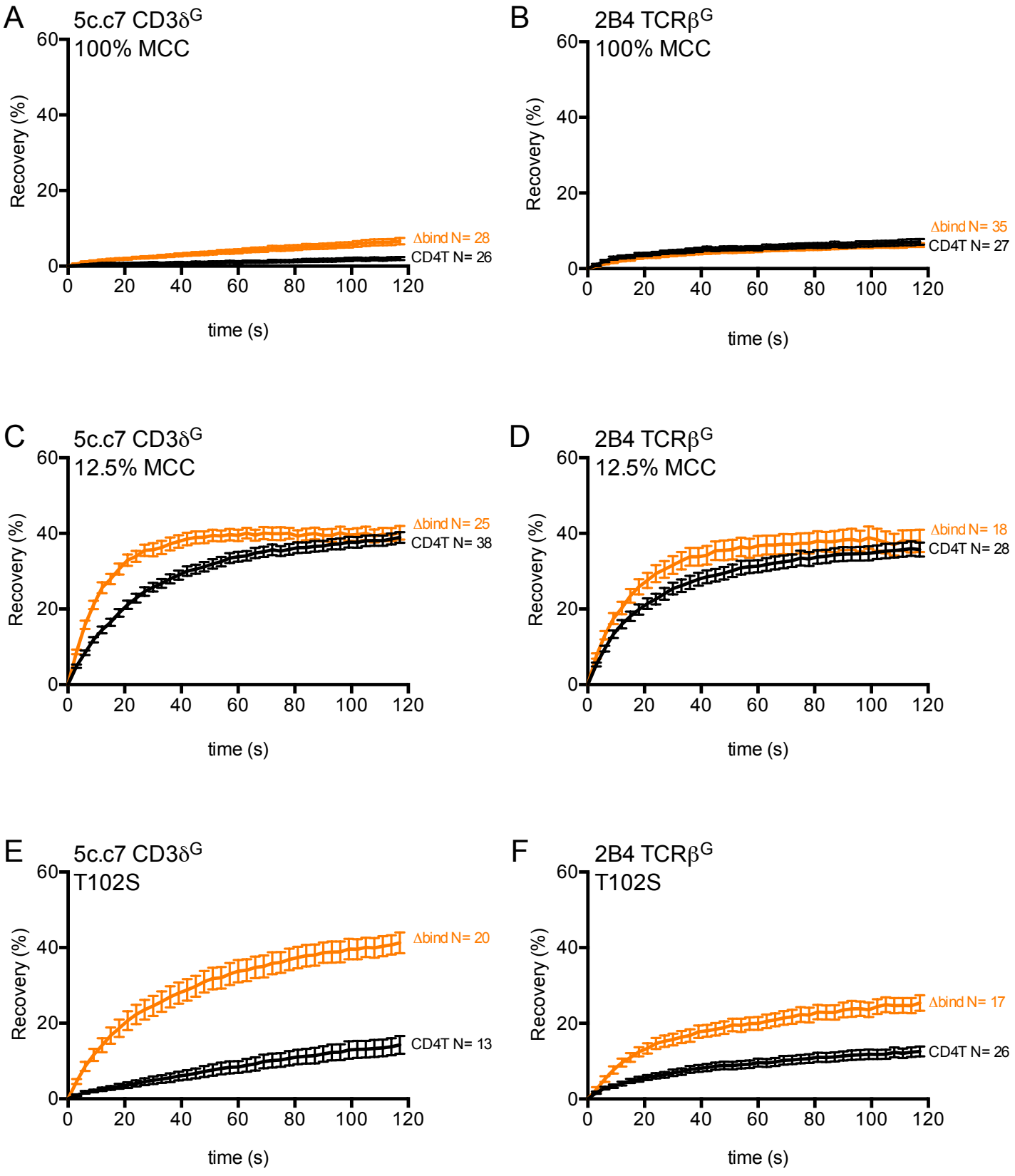
A
5c.c7 CD3δ^G
100% MCC
Recovery (%)
time (s)
Δbind N= 28
CD4T N= 26
B
2B4 TCRβ^G
100% MCC
Recovery (%)
time (s)
Δbind N= 35
CD4T N= 27
C
5c.c7 CD3δ^G
12.5% MCC
Recovery (%)
time (s)
Δbind N= 25
CD4T N= 38
D
2B4 TCRβ^G
12.5% MCC
Recovery (%)
time (s)
Δbind N= 18
CD4T N= 28
E
5c.c7 CD3δ^G
T102S
Recovery (%)
time (s)
Δbind N= 20
CD4T N= 13
F
2B4 TCRβ^G
T102S
Recovery (%)
time (s)
Δbind N= 17
CD4T N= 26

Figure S5

Figure S5. TCR-CD3 recovery, related to Figure 5.
M12 cells were transduced with genes encoding 5c.c7α, 5c.c7β, truncated CD3 subunits with CD3δT^{G} and CD4T^{mCh} or 2B4α, 2B4β^{G}, CD3T and CD4T^{mCh}. **(A-F)** TCR-CD3 recovery traces of M12 cells on immobile surfaces coated with 100% MCC:I-E^{k} (**A-B**), 12.5% MCC:I-E^{k} diluted into Hb:I-E^{k} (**C-D**), or T102S:I-E^{k} (**E-F**). N = number of cells analyzed.

A

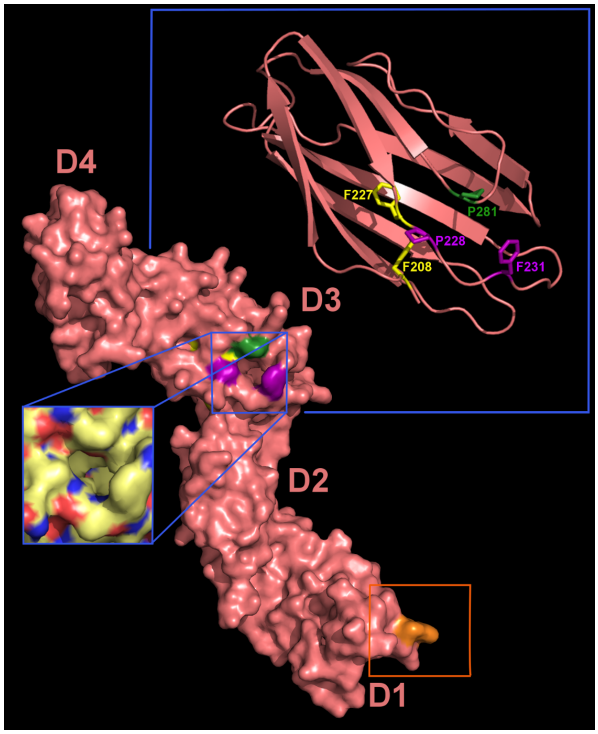

B

Mouse:	FPLNF	Mouse:	GKGVLIR
Rat:	FPLNL	Rat:	NK--LLI
Human:	FPLAF	Human:	GS--FLT
Monkey:	FPLAF	Monkey:	GS--FVT
Cat:	FPLNF	Cat:	HPSLCLT
Dog:	FPLSF	Dog:	GSFWTV-
Goat:	FPLTF	Goat:	NS--FLH
CD4 D3	aa227-231	CD4 D1	aa67-73
WT:	FPLNF	WT:	GKGVLIR
P228E+F231E:	FELNE	Δbind:	GDGDSDS

Mouse:	ETLPL
Human:	KKLPL
Rat:	ETLPL
Monkey:	KKLPF
Cat:	DSLPL
Dog:	ESLPL
Goat:	ERLPL
CD4 D3	aa278-282
WT:	ETLPL
P281E:	ETLEL

C

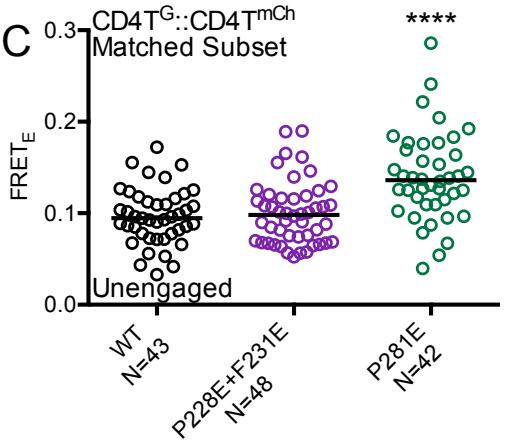

D

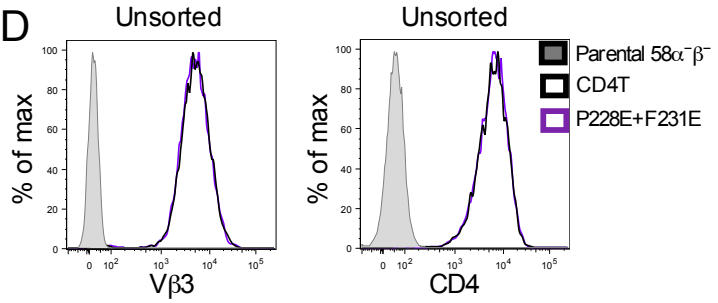

E

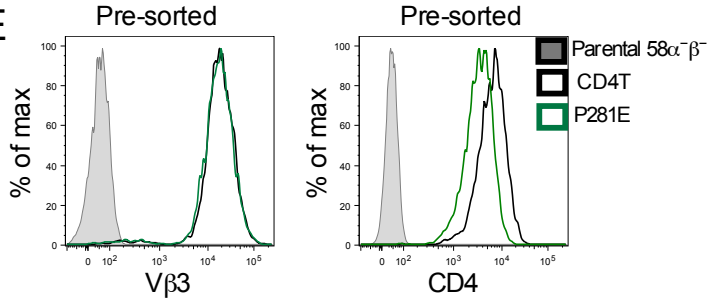

F

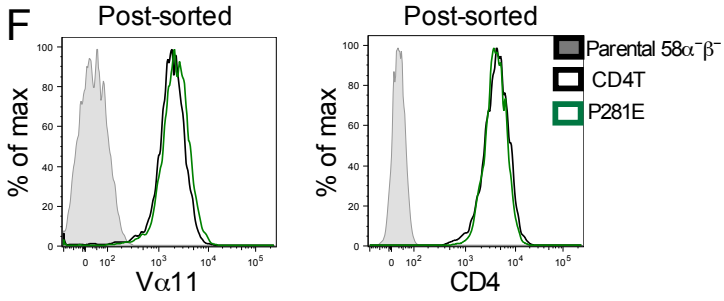

G

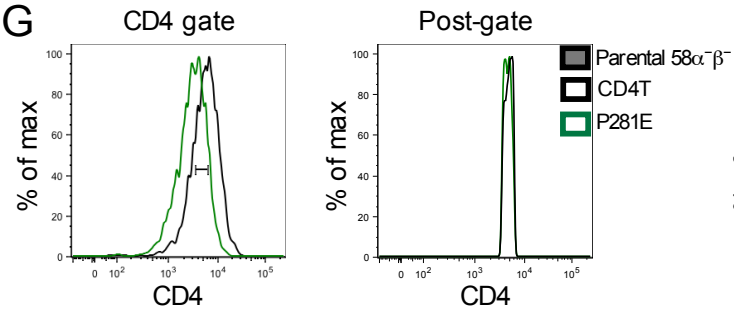

H

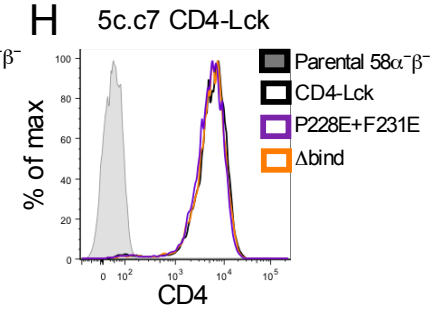

Figure S6

Figure S6. Residues mutated in the CD4 D1 and D3 domains, related to Figure 6.
(**A**) A surface rendered structure of hCD4 (PDB: 1WIO) is shown in Salmon with the D1, D2, D3, and D4 domains labeled. The orange box around residues in the C-terminal D1 domain highlight the MHCII contact site identified in previous structural analysis (Wang et al., 2001; Yin et al., 2012). Orange residues highlight those mutated for the Δbind mutant used in this study (Parrish et al., 2015). The D3 domain solvent exposed residues P228 (purple), F231 (purple), and P281 residues (green) mutated in this study are shown along with the hydrophobic core residues F208 and F227 (yellow) that were previously studied (Vignali and Vignali, 1999). The D3 domain is also shown as a cartoon structure to better highlight these colored residues (upper inset). The nonpolar patch created by P228, F231, and P281 is shown (lower inset) colored by atoms (carbon = yellow, hydrogen = grey, oxygen = red, nitrogen = blue). Images were generated with the PyMOL Molecular Graphics System, Version 1.8 Schrödinger, LLC.
(**B**) Sequence alignment of the CD4 D3 domain residues targeted for mutagenesis. The mutants generated for this study are shown color-coded as in the structure.
(**C**) Donor recovery after acceptor photobleaching of WT or mutant $CD4^{mCh}$::$CD4^{GFP}$ on glass coverslips (unengaged). Data are representative of three independent experiments and were assessed for normality using a D'Agostino and Pearson omnibus normality test followed by a one-way analysis of variance (ANOVA) and Dunnet's multiple comparison test (*$p<0.05$). N = number of cells analyzed.
(**D**) Surface expression of TCR (Vβ3) and CD4 on $5c.c7^{+}58\alpha^{-}\beta^{-}$ cells expressing wild-type CD4 or the P228E+F231E mutations.
(**E**) The P281E mutation reduces CD4 surface expression. (**F**) Sorting for matched expression.
(**G**) Representative example of matched gating used for quantification of CD69 upregulation and TCR downregulation for non-sorted cell lines.
(**H**) Surface expression of CD4 on $5c.c7^{+}58\alpha^{-}\beta^{-}$ cells expressing wild-type CD4-Lck or the P228E+F231E and Δbind mutations.

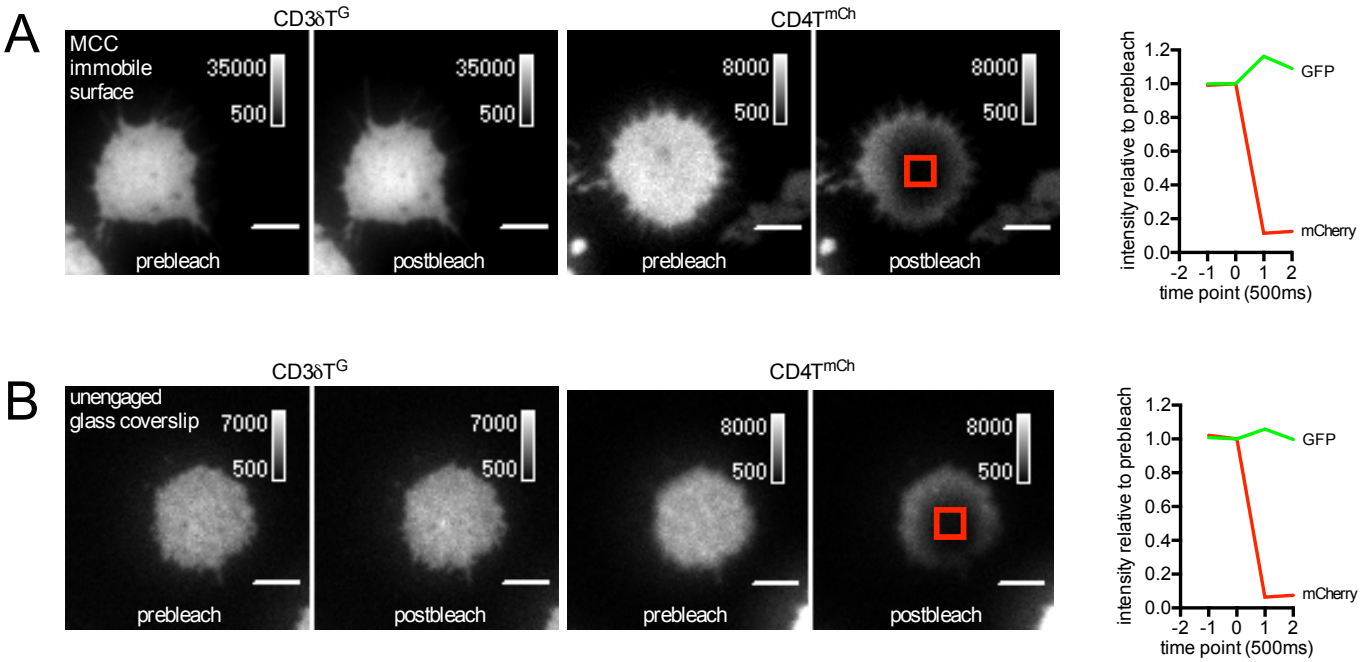
A
CD3δT^G
CD4T^mCh
MCC
immobile
surface
35000
500
8000
prebleach
postbleach
intensity relative to prebleach
GFP
mCherry
time point (500ms)
B
unengaged
glass coverslip
7000

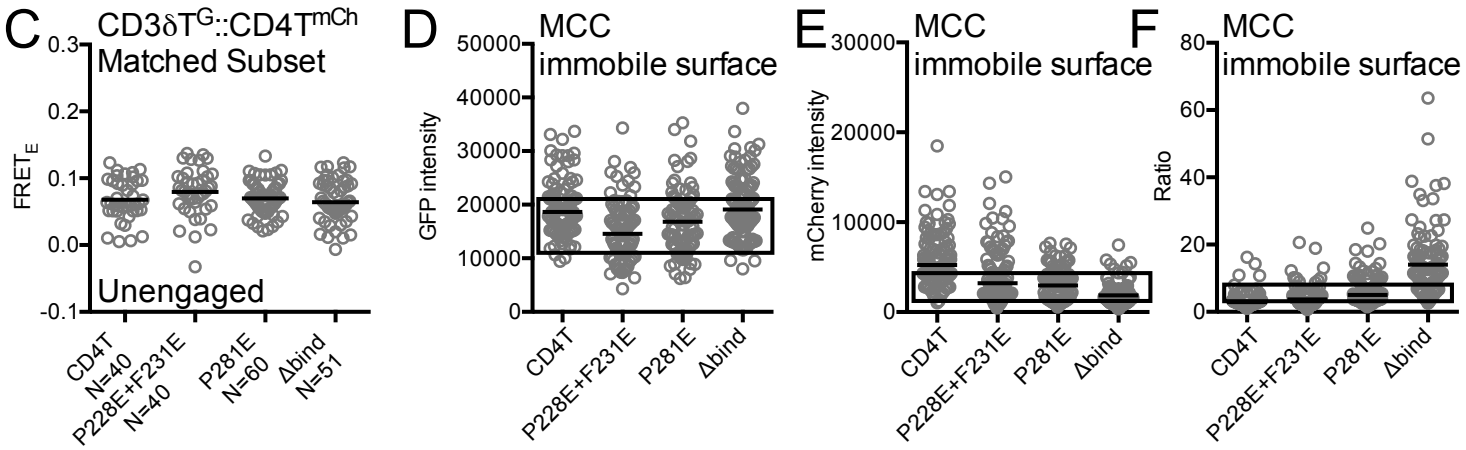
C
CD3δT^G::CD4T^mCh
Matched Subset
FRET_E
Unengaged
CD4T N=40
P228E+F231E N=40
P281E N=60
Δbind N=51
D
MCC
immobile surface
GFP intensity
E
mCherry intensity
F
Ratio

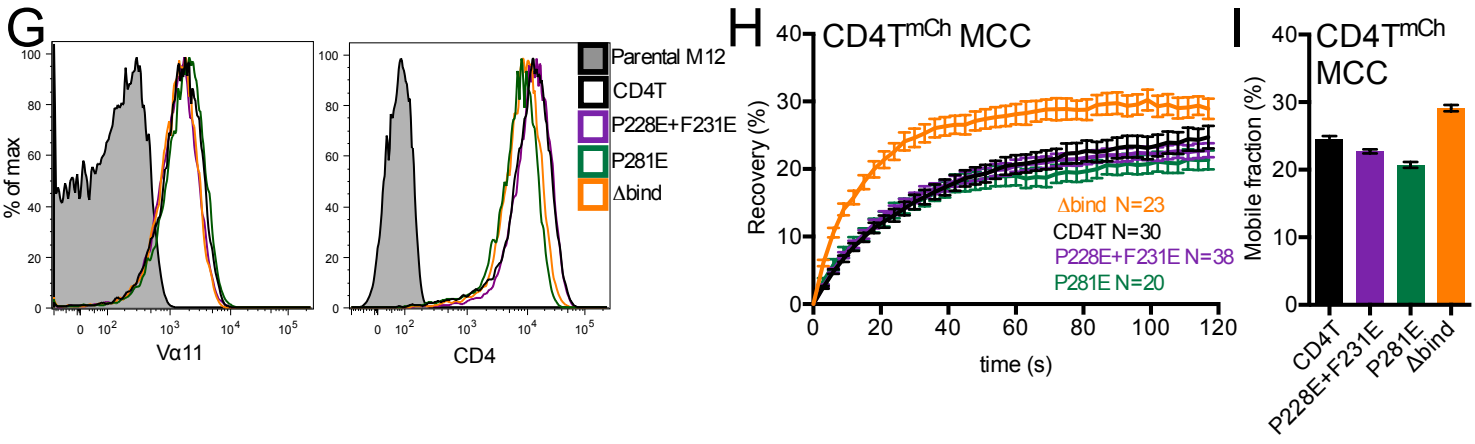
G
% of max
Vα11
CD4
Parental M12
CD4T
P228E+F231E
P281E
Δbind
H
CD4T^mCh MCC
Recovery (%)
time (s)
Δbind N=23
CD4T N=30
P228E+F231E N=38
P281E N=20
I
Mobile fraction (%)

Figure S7

Figure S7. Impact of D3 domain mutants on macrocomplex assembly, related to Figure 7.
(**A-B**) Donor recovery after acceptor photobleaching. Example images and traces are shown for 5c.c7^{+} M12 cells expressing CD3T subunits and CD4T adhered to (**A**) MCC:I-E^{k} coated surfaces, or (**B**) glass coverslips. Background subtracted images show mEGFP (CD3δT^{G}) and mCherry (CD4T^{mCh}) before and after photobleaching. The red box indicates region of interest (ROI). Scale bars represent 5μm and look up tables indicate intensity units for the indicated channels. Traces to the right show mEGFP (green) and mCherry (red) intensities relative to prebleach. Images were acquired at 500ms intervals.
(**C**) Donor recovery after acceptor photobleaching of WT CD4 and mutants on glass coverslips (unengaged). Data are representative of two experiments and were assessed for normality using a D'Agostino and Pearson omnibus normality test followed by a one-way analysis of variance (ANOVA) and Dunnet's multiple comparison test.
(**D-F**) Subset analysis for FRET. Analyzed populations had photobleaching <12.5% of the mCherry prebleach intensity and were matched for (**D**) mEGFP intensity (postbleach), (**E**) mCherry intensity (prebleach) and (**F**) mEGFP/mCherry ratio in TIRF.
(**G**) TCR (Vα11) and CD4 (GK1.5) surface expression on 5c.c7^{+} M12 cells.
(**H-I**) mCherry recovery and mobile fraction of the indicated CD4T mutants adhered to MCC:I-E^{k} coated surfaces. Data are presented as in Figure 3D-E. N = number of cells analyzed.